https://doi.org/10.5194/essd-2026-549
Preprint. Discussion started: 10 September 2026

Open Access Earth System Science Data Discussions

Observations from a 94-GHz spectral polarimetric vertically-pointing radar at Villum research station during the CLAVIER Clean Cloud campaign

Romanos Foskinis[1,2], Anne-Claire Billault-Roux[1,3], Henrik Skov[4], Lise Lotte Sørensen[4], Sven-Erik Gryning[5], Athanasios Nenes[2,6] and Alexis Berne[1]

[1]Environmental Remote Sensing Laboratory, School of Architecture, Civil and Environmental Engineering, École Polytechnique Fédérale de Lausanne, 1015 Lausanne, Switzerland.
[2]Laboratory of Atmospheric Processes and Their Impacts, School of Architecture, Civil and Environmental Engineering, École Polytechnique Fédérale de Lausanne, 1015 Lausanne, Switzerland.
[3]Federal Office of Meteorology and Climatology MeteoSwiss, 1530 Payerne, Switzerland.
[4]Department of Environmental Science, iClimate, Arctic Research Center, Aarhus University, 4000 Roskilde, Denmark.
[5]DTU Wind and Energy Systems, Technical University of Denmark, 4000 Roskilde, Denmark.
[6]Centre for Studies of Air Quality and Climate Change, Institute of Chemical Engineering Sciences, Foundation for Research and Technology Hellas, 26504 Patras, Greece.

Correspondence to: Alexis Berne (alexis.berne@epfl.ch), Romanos Foskinis (romanos.foskinis@epfl.ch)

Abstract. This paper presents a dataset obtained from a ground-based W-band (94 GHz) Doppler spectral polarimetric cloud radar (WProf) during the CLeancloud Arctic VIllum ExpeRiment (CLAVIER) campaign at Villum Research Station, Northeast Greenland, from 23 March to 13 April 2024. The campaign aimed to investigate Arctic cloud microphysical processes and aerosol–cloud interactions under pristine and Arctic haze conditions. Here, we describe the WProf radar measurements and the full processing chain, including noise removal and quality-control filtering, ensuring complete traceability from raw spectra to higher-level products. To resolve the complex microphysical structure of Arctic clouds, the peakTree algorithm was applied to Doppler spectra to identify and characterize multimodal velocity distributions, enabling the detection of coexisting hydrometeor populations within individual radar volumes. Peak-resolved spectral parameters are subsequently used within a hydrometeor classification framework implemented in pyLARDA enabling the identification of liquid droplets, pristine ice crystals, aggregates and rimed particles. The dataset captures a wide range of Arctic spring cloud regimes, including persistent mixed-phase clouds, deep and shallow ice-precipitating systems, and vertically structured seeder–feeder configurations. The observations indicate that multimodality is a common feature of Arctic clouds, particularly during periods of active ice growth, aggregation, and cloud-layer interaction. As dynamic forcing weakens, cloud systems frequently evolve toward shallower and more homogeneous stratiform states with reduced spectral complexity. Overall, the dataset provides a solid basis for studying Arctic aerosol-cloud interactions and cloud microphysics for evaluating the cloud and precipitation parameterizations in models.

https://doi.org/10.5194/essd-2026-549
Preprint. Discussion started: 10 September 2026

Open Access Earth System Science Data Discussions

1 Introduction

Arctic clouds play a key role in the global climate system, strongly influencing surface radiation budgets, atmospheric stability, and the evolution of sea ice. These clouds are predominantly persistent and mixed-phase in nature—composed of coexisting supercooled liquid water droplets and ice crystals—and span a wide variety of vertical structures, ranging from shallow boundary-layer clouds to deep, vertically extensive systems. Their microphysical complexity, particularly the interplay between cloud condensation nuclei, ice-nucleating particles, and radiative processes, significantly modulates the Arctic energy balance and contributes to strong cloud feedback in a warming climate (Lohmann & Neubauer, 2018; Tan & Storelvmo, 2019). Despite their critical importance, Arctic mixed-phase clouds remain poorly understood and represented in global climate models, due to largely persistent uncertainties in cloud microphysical processes and aerosol-cloud interactions (Wallentin et al., 2025). These knowledge gaps not only hinder accurate simulation of Arctic climate change but also amplify uncertainty in projections of sea-ice decline and regional radiative forcing (Morrison et al., 2011; Tan et al., 2023).

Recent observational studies have demonstrated that Arctic cloud and precipitation characteristics exhibit pronounced variability driven by synoptic-scale dynamics, aerosol concentrations, and the underlying thermodynamic structure of the atmosphere (Moser et al., 2023). Complex microphysical interactions—such as seeder–feeder processes, riming, and aggregation—are frequently observed under Arctic conditions, especially within multilayer cloud systems where vertically separated cloud layers interact via falling ice particles (Wallentin et al., 2025). These interactions contribute to the formation of diverse hydrometeor populations within individual cloud systems, including supercooled droplets, ice crystals, and graupel.

Ground-based cloud radars operating at millimeter wavelengths offer continuous and highly sensitive observations of Arctic clouds and are therefore essential for advancing process-level understanding. W-band (i.e. around 95 GHz) Doppler cloud radars enable the detection of both liquid cloud droplets, ice crystals and weak ice precipitation, making them well suited for Arctic applications. However, traditional analyses based on radar moments may mask the presence of multiple particle populations, which are instead manifested as multimodal structures in Doppler velocity spectra. Recent advances in Doppler spectral analysis enable the identification of distinct velocity modes associated with different hydrometeor populations. Spectral decomposition techniques, such as the peakTree algorithm (Radenz et al., 2019), the pyPEAKO (Kalesse et al., 2019; Billault-Roux et al., 2023) or a combination of both Vogl et al. (2024), enable the systematic characterization of multimodal Doppler signatures; when combined with physically based classification schemes, they provide new opportunities to investigate Arctic cloud microphysics beyond what is accessible from moment-based products alone.

Early applications of ground-based cloud radars in the Arctic focused primarily on continuous observations of cloud structure and dynamics using vertically pointing millimeter-wavelength systems. During the Surface Heat Budget of the Arctic Ocean (SHEBA) experiment (1997–1998), one of the first vertically pointing Ka-band (~35 GHz) cloud radars was deployed on an icebreaker frozen into the Arctic sea ice, enabling continuous, year-long observations of Arctic clouds (Uttal et al., 2002). The radar collected measurements of cloud reflectivity and Doppler velocity, allowing the vertical structure and temporal evolution of clouds to be monitored. Although higher-frequency W-band radars and advanced spectral techniques were not widely used

https://doi.org/10.5194/essd-2026-549
Preprint. Discussion started: 10 September 2026

by that time, the SHEBA cloud radar dataset represented one of the first long-term millimeter-wavelength radar records in the Arctic and laid the foundation for current understanding of persistent Arctic mixed-phase clouds. Then, several Arctic field campaigns have been conducted to improve our current understanding of cloud processes through the collection of high-quality cloud datasets. Long-term ground-based remote sensing observations at Ny-Ålesund, using a vertically pointing 94 GHz cloud radar together with a 35 GHz dual-polarization scanning one, have collected measurements spanning more than one year and enabled robust analyses of low-level Arctic mixed-phase cloud structure and variability (e.g., Chellini et al., 2023). Additionally, large and intensive campaigns such as ACSE (2014; ~3 months), AO2018 (2018; ~6 weeks) (Vüllers et al., 2021), and MOSAiC (2019–2020; one full year) on board of the icebreaker Polarstern combined ground-based remote sensing, in situ observations, and modeling to provide extended characterizations of Arctic clouds, aerosols, and radiation under drifting-ice conditions and at high-latitude supersites such as Ny-Ålesund (79ºN) and Utqiaġvik (71º) (Achtert et al., 2025). In parallel, the long-term NASCENT campaign at Ny-Ålesund (Pasquier et al., 2022) used the Cloudnet target classification product (Illingworth et al., 2007) and demonstrated how the low-level mixed-phase clouds are dominating year-round at Ny-Ålesund, underscoring the climatic importance of persistent Arctic mixed-phase clouds (Pasquier et al., 2022).

Beyond moment-based analyses, Doppler spectral approaches have also been applied to Arctic mixed-phase clouds (Luke et al., 2021). Verlinde et al. (2013) analyzed millimeter-wave cloud radar Doppler spectra from the M-PACE campaign (2004; ~1 month) (Vüllers et al., 2021) over the North Slope of Alaska and showed that the multimodal structure of Doppler spectra can be used to identify distinct velocity modes associated with cloud droplets, drizzle, and different ice populations, allowing coexisting hydrometeors within a single radar volume to be separated. Their case-study-based analysis demonstrated how spectral modes provide insight into key microphysical processes, such as drizzle formation, ice precipitation from above, and secondary ice production, and laid the groundwork for later peak-resolved spectral approaches.

The dataset presented here further advances Arctic cloud observations by providing, for the first time, vertically pointing W-band cloud radar measurements during CLeancloud Arctic VIllum ExpeRiment (CLAVIER) at Villum Research Station (VRS) in Northeast Greenland (81°36' N, 16°40' W), from 23 March to 13 April 2024. Villum has long hosted extensive aerosols, radiation, and meteorological observations, while cloud remote sensing at the site has previously been limited to ceilometer measurements (Gryning et al., 2023). The observational period was selected to coincide with the spring-to-summer transition at VRS, a location situated at the transition between the Arctic Ocean and land. This period represents a critical phase for Arctic cloud evolution, characterized by rapid changes in thermodynamic structure, surface conditions, and radiative forcing. During this time, Villum is frequently influenced by long-range aerosol transport events as well as episodic heat and moisture intrusions into the high Arctic, all of which can strongly affect cloud phase, persistence, and precipitation processes. The one-month deployment of the W-band Doppler cloud radar during CLAVIER therefore aimed to collect a unique information of how these cloud regimes evolve by measuring the vertically resolved, peak-separated Doppler spectra.

The W-band Doppler cloud radar collects vertically resolved reflectivity and peak-resolved Doppler spectra, enabling the characterization of coexisting hydrometeors along the atmospheric profile. The CLAVIER radar dataset enhances existing Arctic cloud observations by incorporating detailed W-band Doppler spectral information, supporting improved representation

https://doi.org/10.5194/essd-2026-549
Preprint. Discussion started: 10 September 2026

Open Access Earth System Science Data Discussions

of Arctic mixed-phase cloud microphysics at a location devoids of such observations so far. This spectral capability allows for the identification of multimodal velocity structures and mode-specific hydrometeor classifications, offering a valuable benchmark for evaluating advanced microphysical parameterizations and radar forward operators.
In this study, we present a W-band Doppler cloud radar dataset that includes peak-resolved spectral products derived using the peakTree algorithm, along with hydrometeor classifications from pyLARDA, distinguishing liquid droplets, pristine ice, aggregates, rimed particles, and mixed-phase conditions.

2 Experimental site & CleanCloud CLAVIER campaign

The CLAVIER campaign was conducted at VRS (81.6° N, 16.7° W) in Northeast Greenland (https://villumresearchstation.dk), one of the northernmost continuously operated research stations worldwide and an ACTRIS and ICOS site coordinated by Aarhus University (Figure 1). The station is located in a remote High-Arctic environment characterized by minimal local anthropogenic aerosol sources and frequent transitions between pristine and Arctic haze conditions (Heidam et al., 2004; Nguyen et al., 2013; Lange et al., 2018), making it well suited for studying aerosol–cloud interactions and Arctic cloud microphysics. CLAVIER campaign was carried out during the Arctic Spring as part of the Horizon Europe project CleanCloud. (https://projects.au.dk/cleancloud/cleancloud-project, Clouds and climate transitioning to post-fossil aerosol regime). CleanCloud brings together 20 European research institutes with expertise in ground-based and satellite remote sensing, in situ observations, laboratory experiments, and atmospheric and climate modelling. The overarching aim of the project is to improve the understanding and representation of aerosol–cloud interactions as the climate system transitions towards a post-fossil aerosol regime, and to reduce related uncertainties in climate predictions.

https://doi.org/10.5194/essd-2026-549
Preprint. Discussion started: 10 September 2026

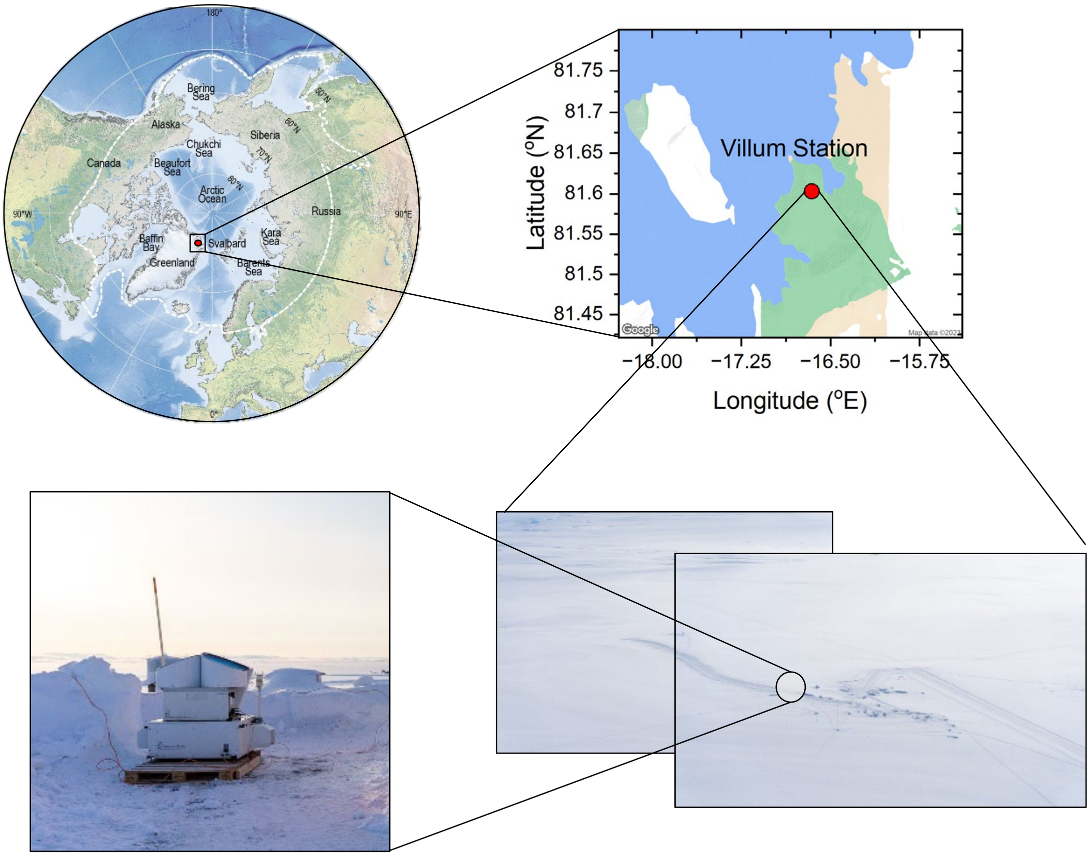

Figure 1: The Arctic overview map and the regional map of Northeast Greenland show the location of VRS located at Station Nord. The lower panels show the W-band Doppler cloud radar installation at the site and a view of the surrounding terrain.

Within CleanCloud, the CLAVIER campaign was the first coordinated effort to contribute to the scientific cluster on aerosol and cloud processes in an extreme Arctic environment. The campaign involved multiple CleanCloud partners and combined ground-based remote sensing together with in situ and auxiliary observations to characterize aerosol properties, cloud microphysics, and dynamical conditions. These observations form the basis of the dataset presented in this study and support the investigation of Arctic cloud processes relevant to aerosol–cloud interactions and the evaluation of remote-sensing retrievals.

3 Instrumentation and ancillary data

3.1 W-band cloud radar (WProf)

A vertically pointing W-band Doppler cloud radar, hereafter referred to as WProf, was deployed at VRS during the CLAVIER campaign. WProf is a frequency-modulated continuous-wave (FMCW) Doppler spectral zenith profiler developed by Radiometer Physics GmbH (RPG; Küchler et al., 2017), providing measurements of radar moments, full Doppler reflectivity

https://doi.org/10.5194/essd-2026-549
Preprint. Discussion started: 10 September 2026

spectra, and polarimetric information in the form of co- and cross-polarized returns, from which the linear depolarization ratio (LDR) was derived throughout the campaign. The instrument metadata are publicly available through the ACTRIS Cloudnet Portal (Berne and Foskinis, 2026a). The radar configuration employed a three-chirp setup, dividing the vertical profile into consecutive range sections to maintain high sensitivity throughout the measurement domain. This configuration provides higher vertical and Doppler velocity resolution close to the surface, with progressively reduced resolution at higher altitudes to ensure sufficient sensitivity in the upper part of the profile, consistent with the expected decrease in vertical air motion and particle fall velocities with height in Arctic cloud systems. The main technical characteristics of the radar system and the adopted configuration are summarized in Table 1. Although the measurements were affected by a small coherent polarimetric leakage, corresponding to an effective receiver misalignment of about 2°, this effect was explicitly quantified (A. Myagkov, RPG, personal communication). Assuming a simple rotation of the polarization basis, such a misalignment leads to a cross-channel leakage proportional to sinθ, yielding an amplitude coupling of sin(2°) ≈ 0.035 (≈3.5%), corresponding to ~0.12% in power. This leakage sets an instrumental lower bound on the linear depolarization ratio of 10log10(0.0012) ≈−29 dB. The instrument was calibrated and performance-checked according to the manufacturer's procedures both before and after the campaign, confirming stable and proper instrument operation throughout the observation period. Additionally, we provide the 2-dimensional histogram in Figure 2 of the attenuated equivalent reflectivity factors recorded by WProf.

	WProf
Frequency (GHz)	94
Radar type	FMCW Doppler spectral zenith profiler
3 dB beam width (°)	0.56
Time resolution (s)	4.714
Sensitivity	Derived ≈ −43.6 dB (0.9 km) | −39.7 dB (3 km) | −30.8 dB (8 km)
Range resolution (m)	14.9 | 34.1 | 35.8
Nyquist velocity (m s^{-1})	10.94 | 7.25 | 5.09
Velocity resolution (m s^{-1})	0.021 | 0.014 | 0.010
Chirp 0 range (m)	104–894
Chirp 1 range (m)	920–2998
Chirp 2 range (m)	3005–9981

Table 1: Properties and parameters of the ground-based W-band Doppler cloud radar WProf operated during CLAVIER. WProf uses three FMCW chirps with different range coverages; when applicable, values are reported separately for each chirp, respectively.

https://doi.org/10.5194/essd-2026-549
Preprint. Discussion started: 10 September 2026

Open Access Earth System Science Data Discussions

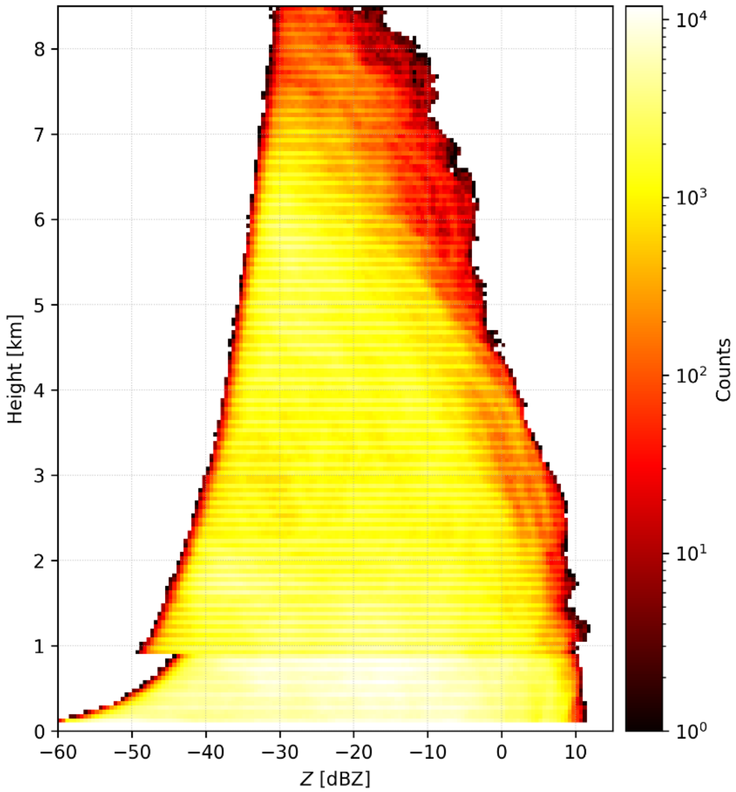

Figure 2: Two-dimensional histogram of the equivalent radar reflectivity factor measured by WProf across all cloud events, with a minimum signal-to-noise ratio (SNR) threshold of 0 dB applied. The processing approach is detailed in Appendix B.

3.2 Meteorological Measurements

The wind speed and direction were obtained from a meteorological mast (climate mast) at 9 m above ground level, located next to the monitoring house, approximately 2 km outside Station Nord. We chose to use the wind data from the climate mast because its measurements are considered representative of the surrounding area and are not influenced by nearby buildings or local structural disturbances. The ground temperature pressure, and relative humidity (with respect to liquid water) were obtained from the Vaisala WXT536 meteorological station mounted directly on the WProf system. Additionally, we estimated the relative humidity with respect to ice at ground level using the formulation of Murray (1967). Case-specific meteograms combining these measurements are presented in Appendix A4. For example, Figure D1 shows the temperature, pressure, wind speed and direction, and relative humidity with respect to water and ice for the period 23–25 March 2024.

4 Methodology

The data processing workflow applied in this study consists of four sequential steps. First, the Doppler radar spectra were subject to a spectral post-processing procedure to remove noise and spurious signal contributions. Subsequently, the peakTree

https://doi.org/10.5194/essd-2026-549
Preprint. Discussion started: 10 September 2026

algorithm (Radenz et al., 2019) was applied to the corrected spectra to identify and isolate multimodal Doppler spectral structures, enabling the separation of distinct peak-resolved components within individual radar volumes. Finally, these peak-resolved spectral components were used as input to the pyLARDA hydrometeor classification scheme (Bühl et al., 2021), which was employed to classify liquid droplets, pristine ice, aggregates, rimed particles, and mixed-phase conditions. Thus, this paper provides data that makes it possible to quantitatively investigate the importance and the added value of identifying peak-resolved hydrometeor populations from Doppler spectral observations. The obtained classifications reveal pronounced temporal and vertical variability in hydrometeor type, reflecting the complex and rapidly evolving microphysical structure of Arctic cloud systems. This information highlights the potential of having peak-resolved radar-based approaches to provide physically meaningful insight into cloud phase composition and microphysical processes.

4.1 Spectral post-processing of Doppler radar data

As a first step in the data processing workflow, the Doppler radar spectra were subjected to a spectral processing procedure (Hildebrand & Sekhon, 1974) designed to suppress noise contributions before the spectral peak detection. Then, spectral peak detection was performed independently for each radar chirp using chirp-specific averaging, smoothing, and detection parameters, as detailed in Appendix B. Doppler spectra were first smoothed and then filtered using adaptive noise thresholds that were estimated independently for each chirp. Noise filtering was applied to the co- and cross-polarized channels before computing the LDR, and spectral bins dominated by noise were excluded. Peaks were then identified within predefined Doppler velocity ranges using simple prominence criteria, allowing for multiple spectral modes per time–range gate. A detailed description of the processing steps is provided in the Appendix B. The gas attenuation was obtained from the CloudnetPy module (Tukiainen et al., 2020), in which it is calculated as the specific attenuation due to atmospheric gases according to the International Telecommunication Union (ITU-R P.676). Temperature, pressure, and water-vapor profiles were derived from ERA5 reanalysis data (Hersbach et al., 2018) and extrapolated to the radar height bins. These variables were used to compute frequency-dependent absorption by dry air (primarily oxygen) and water vapor using standard ITU parameterizations. The total gas attenuation was obtained as the sum of the oxygen and water-vapor contributions and scaled by frequency (here 94 GHz) to yield specific attenuation in dB km^{-1}. Overall, the maximum specific two-way gas attenuation during the campaign was 9.5×10^{-5} dB km^{-1}, which is negligible; therefore, no additional correction was applied to the reflected radar signal. The potential attenuation due to supercooled liquid water was also assessed. Two periods (Case 1-5 and 11-13 of April) were identified during which attenuation from cloud and precipitation particles, including supercooled liquid water droplets, was enhanced. However, even during these events, the maximum total attenuation remained limited to approximately 1.5–2 dB at about ~9 km.

4.2 Identification of multimodal Doppler spectra

The peakTree algorithm was applied to the WProf Doppler spectra to identify multimodal structures in the Doppler spectral space. The peakTree is an algorithm designed to describe multi-peaked Doppler spectra without assuming a fixed number of

https://doi.org/10.5194/essd-2026-549
Preprint. Discussion started: 10 September 2026

peaks. It works by recursively splitting the Doppler spectrum at a local minimum, organizing the resulting spectral components into a binary tree structure. In this representation, a node corresponds to a spectral component defined over a Doppler velocity interval; the root node represents the full spectral signal, while child nodes represent sub-components created by successive spectral splits. Leaf nodes are the final nodes that cannot be further split and therefore represent individual spectral peaks. In this framework, the spectral modes discussed in this study correspond to the leaf nodes of peakTree and are interpreted as signatures potentially associated with distinct hydrometeor populations within a single radar volume.

Then, for each identified spectral mode, the radar equivalent reflectivity factor (Ze_m), mean Doppler velocity (v_m), spectral width, signal-to-noise ratio (SNR), and linear depolarization ratio (LDR_m) were retrieved. Only peaks that meet the criteria described in the Spectral Postprocessing Procedure in the Appendix B are retained.

To illustrate the temporal and vertical evolution of the detected multimodality, the figures in Appendix A5, such as Figure E1, present time–height cross-sections of Ze_m, v_m, LDR_m, and the temporal standard deviation of v_m calculated over a ±5 min window for up to three retained spectral modes. Mode 0 denotes the dominant spectral peak, whereas modes 1 and 2 denote additional, generally weaker peaks detected within the same radar sampling volume. Blank regions indicate that no valid peak satisfying the post-processing criteria was identified. The mode number does not correspond to a fixed hydrometeor class or to a population continuously tracked through time. Additionally, the corresponding boxplots in Appendix A5, such as Figure E2, summarize the distributions of Ze_m, LDR_m, and v_m for Modes 0–3, together with the number of radar volumes contributing to each mode. The boxes represent the interquartile range and median, while the whiskers show the data spread excluding outliers. These complementary figures show where and when multimodality occurs and enable the spectral and polarimetric properties of the secondary modes to be compared with those of the dominant mode while accounting for their different occurrence frequencies.

This configuration enables robust identification of vertically stratified hydrometeor populations in multilayer and mixed-phase Arctic cloud systems. For instance, Figure 2 illustrates the application of the peakTree algorithm to representative Doppler spectra from the three radar chirps. After preprocessing and noise filtering, peakTree identifies local maxima in the co-polarized spectra and recursively separates them into individual spectral components. In the examples shown (Figure 3), the cross markers indicate the spectral peaks detected by peakTree. Each detected peak corresponds to a leaf node of the peakTree and represents a distinct spectral mode, interpreted here as a separate hydrometeor population coexisting within the same radar sampling volume.

https://doi.org/10.5194/essd-2026-549
Preprint. Discussion started: 10 September 2026

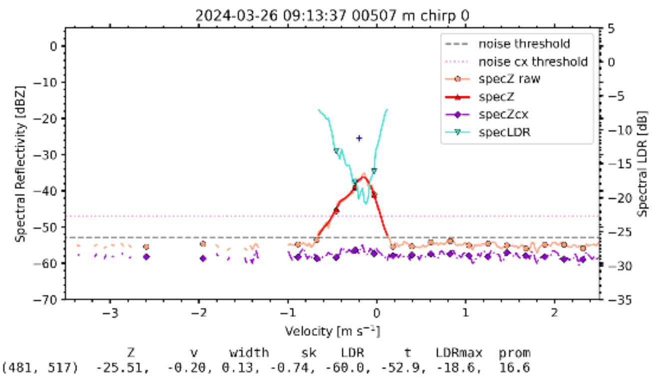

a)

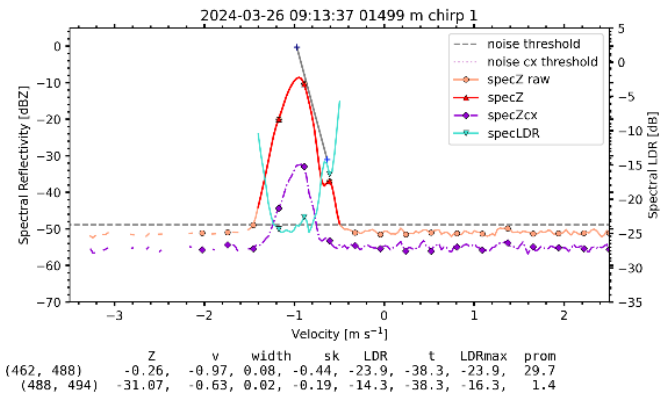

b)

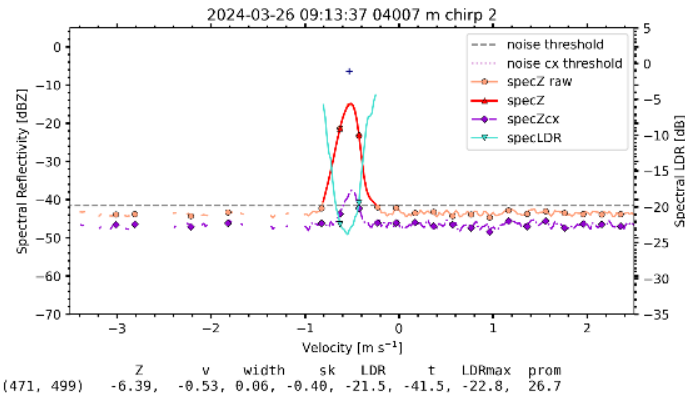

c)

Figure 3: Examples of Doppler spectra and peakTree peak detection for the three radar chirps at Villum Research Station on 26 March 2024 at 09:13:37 UTC. Panels (a), (b), and (c) show representative spectra from chirps 0, 1, and 2, respectively. For each chirp, the co-polarized Doppler spectrum after preprocessing and smoothing (specZ) is shown together with the raw co-polarized spectrum (specZ raw) and the cross-polarized spectrum (specZcx). The derived linear depolarization ratio spectrum (specLDR) is displayed on the same Doppler velocity axis. Horizontal dashed lines indicate the estimated noise level and the corresponding detection threshold used for peak identification. Cross markers denote spectral peaks detected by the peakTree algorithm.

4.3 Hydrometeor classification based on spectral modes

The hydrometeor classification scheme was applied afterwards to the peak-resolved products using the pyLARDA framework. The application of peakTree to the Doppler spectrum enables the identification and tracking of multimodal velocity signatures, allowing the detection of coexisting hydrometeor populations within individual radar volumes. The resulting peak-based parameters, combined with radar moments and auxiliary thermodynamic information, are used to classify liquid droplets, pristine ice, aggregates, rimed particles, and mixed-phase conditions. More details can be found in Appendix C.

https://doi.org/10.5194/essd-2026-549
Preprint. Discussion started: 10 September 2026

5 Overview of the dataset

This section presents an overview of the WProf radar dataset during the CLAVIER campaign, including its temporal coverage, vertical extent, and key characteristics of the peak-resolved Doppler spectral products. The overview focuses on the seven identified cloud cases, spanning the periods 1) 23–25 March, 2) 25–26 March, 3) 27 March, 4) 28–31 March, 5) 1–5 April, 6) 8 April, and 7) 11–13 April 2024 that were captured during the campaign and they will be used to illustrate the diversity of multimodal Doppler signatures captured as well as the highlights of the cloud's structure.

5.1 Case 23–25 March 2024

During 23–25 March 2024, an extensive and persistent cloud system associated with a warm-air intrusion driven by a low-pressure system was observed over VRS (Fig. D1). As shown in Figure 4, the cloud initially spans from a base near 3 km to a top of approximately 6 km. It subsequently lowers, with the cloud base descending toward the surface, while the cloud deepens and the cloud top rises to around 7 km. During the later stage, the cloud base gradually lifts back to approximately 3 km, while the cloud remains vertically extensive. Near the cloud top, intermittent layers of weak reflectivity, near-zero Doppler velocity, and very low LDR are observed, which may indicate the presence of persistent supercooled liquid layers not captured by the classification procedure. Figure 4 d, e and f show that the cloud is mostly dominated by a single Doppler mode, which translates to a single population found as fastest falling and columnar crystals throughout the cloud column and occasionally a second mode of crystal was captured. Additionally, larger ice aggregates were also captured during phases of cloud deepening. Fig. E1 and E2 further demonstrate that secondary Doppler modes exhibit lower reflectivity, weaker terminal velocities, and LDR highlighting vertically and temporally distinct hydrometeor populations within the cloud. Additionally, the spectrogram at 23:59 UTC on 23 March 2024 (Fig. F1) shows a relatively narrow, predominantly single-mode ice signature between approximately 1.5 and 4 km, with fall velocity increasing towards lower altitudes. Below about 1–1.5 km, the spectrum broadens and separates into a second mode with distinct Ze and LDR signatures, which the hydrometeor classification classifies as a continuous fastest-falling population accompanied primarily by a columnar ice mode. This illustrates the increasing microphysical complexity of the cloud towards the surface.

https://doi.org/10.5194/essd-2026-549
Preprint. Discussion started: 10 September 2026

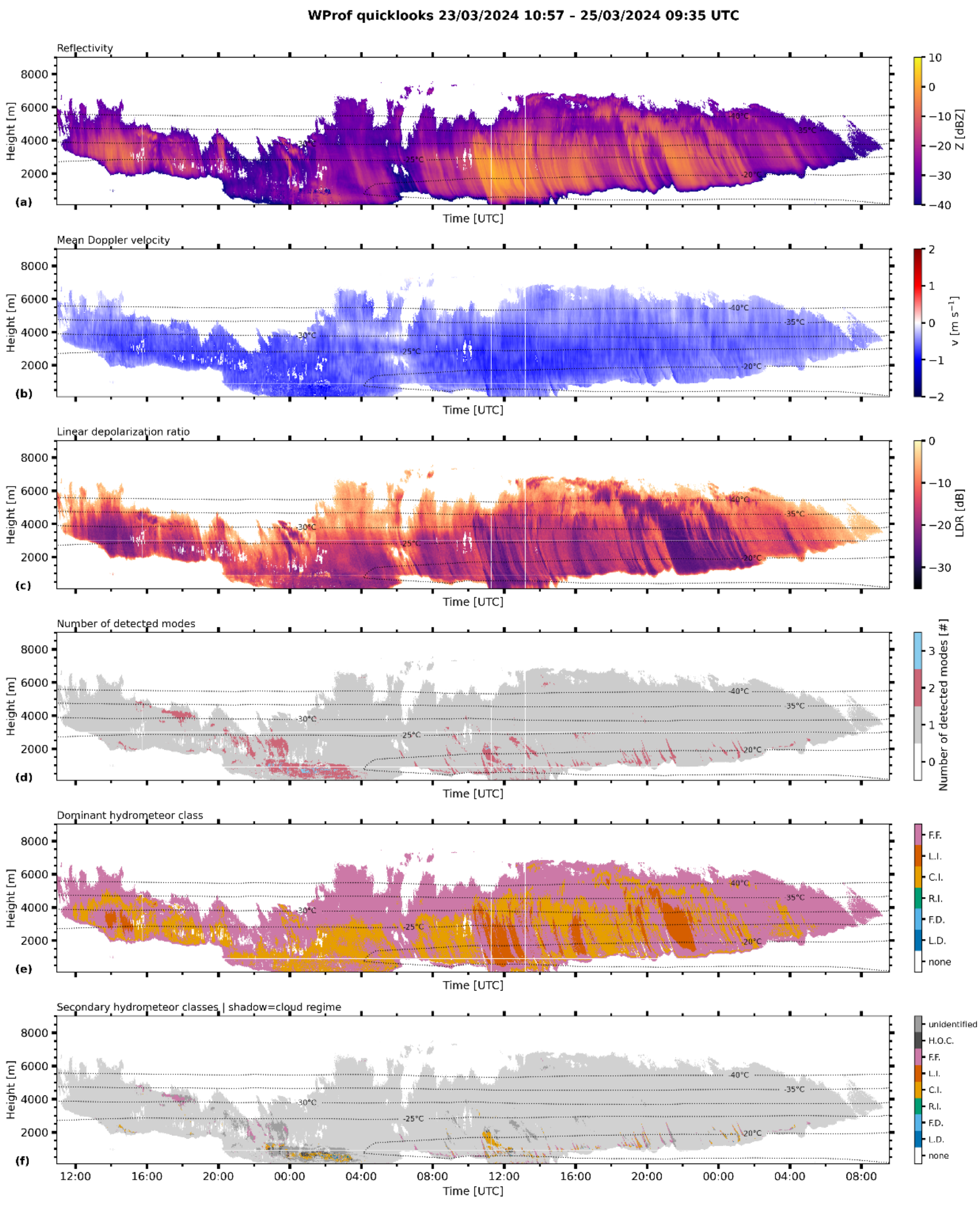

Figure 4: Time–height cross sections of WProf observations of the dominant spectral mode from 23 March 2024, 10:57 UTC to 25 March 2024, 09:35 UTC: (a) equivalent radar reflectivity factor, (b) mean Doppler velocity, (c) linear depolarization ratio (LDR), and (d) number of spectral modes detected by the PeakTree algorithm. The occurrence of multiple spectral modes indicates the coexistence of distinct hydrometeor populations. (e) Time–height distribution of the dominant hydrometeor class and (f) distribution of secondary classes and their combinations, where present. Hydrometeor classes are defined as: F.F. — fastest-falling particles; L.I. — large ice; C.I. — columnar ice; R.I. — rimed ice; F.D. — frozen drops; L.D. — liquid droplets; H.O.C. — higher-order combinations (more than two coexisting modes); and unidentified when the observed mode does not match any predefined pyLARDA class. Temperature contours (°C) derived from ERA5 are overlaid on all panels.

https://doi.org/10.5194/essd-2026-549
Preprint. Discussion started: 10 September 2026

Open Access Earth System Science Data Discussions

5.2 Case 25–26 March 2024

During 25–26 March 2024, the cloud initially developed at higher altitudes and subsequently deepened toward the surface following by a rapid drop in surface pressure and temperature (Fig. D2). At the beginning of the period, the cloud is confined to upper levels and is dominated by columnar ice, as indicated by the hydrometeor classification and elevated LDR values (Figure 5). As the cloud deepened, radar reflectivity increases and Doppler velocities increase (Figure 5), indicating ice growth and the onset of precipitation. Over time, large ice particles become dominant within the descending precipitation shaft. Figure 5 d, e and f show pockets in which a second mode of columnar ice crystals coexisted with the surrounding large ice particles. The spectrogram at 08:32 UTC on 26 March 2024 (Fig. F2) illustrates this structure, showing the cloud extend from near the surface to approximately 6.8 km, a dominant large-ice mode below about 4 km, and a slower secondary columnar-ice mode that is particularly evident around 2.4–2.8 km. After the main precipitation event around 8–9 UTC, a shallow low-level cloud remains near the surface for a few hours. This residual cloud is characterized by weak reflectivity, near-zero Doppler velocities, and low LDR values. The hydrometeor classification confirms liquid water in this low-level cloud persists after the decay of the precipitating ice system. In addition, the boxplots (Fig. E4) show clear differences between spectral modes: the dominant mode exhibits higher reflectivity, faster fall speeds, and lower LDR values, while higher-order modes show lower reflectivity, slower fall speeds, and higher LDR values.

https://doi.org/10.5194/essd-2026-549
Preprint. Discussion started: 10 September 2026

Open Access Earth System Science Data Discussions

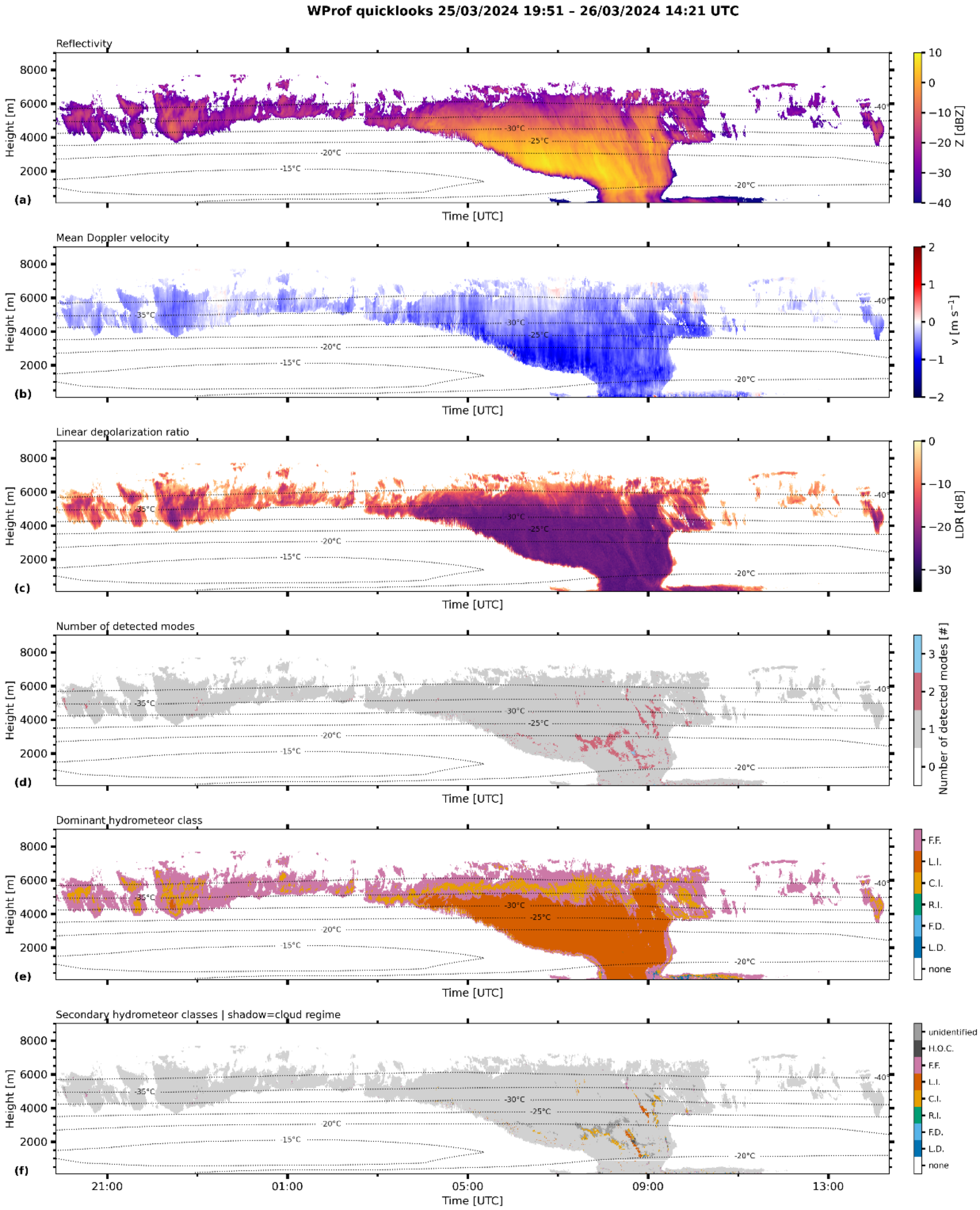

Figure 5: Same as Figure 4 for the period 25 March 2024 19:51 – 26 March 2024 14:21 UTC.

5.3 Case 27 March 2024

On March 27th a short-lived and vertically confined cloud system accompanied by a gradual increase in both near-surface air temperature and pressure possibly associated with a warm-air intrusion was observed (Fig. D3). The cloud is mainly located

https://doi.org/10.5194/essd-2026-549
Preprint. Discussion started: 10 September 2026

around 2km above ground level and shows moderate radar reflectivity together with predominantly downward Doppler velocities, indicating ice particles and weak precipitation (Figure 6). Ice crystals likely form near this layer and precipitate downward. The spectrogram at 11:56 UTC (Fig. F3) shows columnar ice near the cloud top at approximately 1.8 km. Towards lower levels, the Doppler velocities become more negative and fast-falling and large-ice particles appear, indicating increasing particle fall speeds. Below approximately 500 m, a distinct second mode indicates the presence of an additional hydrometeor population. Enhanced turbulence is observed below (Fig. F3) the cloud top in the Doppler spectra, consistent with radiative cooling at the cloud top driving turbulent buoyant mixing in the underlying cloud layer. Figure 6d shows frequent detection of multiple Doppler spectral modes, indicating the coexistence of different hydrometeor populations. Figure 6 d, e and f show that the cloud is dominated by fast-falling and large ice. Liquid droplets and columnar are detected only intermittently, primarily near the cloud top and just below the cloud base, while localized pockets of larger ice particles are observed at around 1 km altitude. The absence of these larger ice particles at lower levels may indicate three-dimensional dynamical effects, whereby the particles are advected out of the radar sampling volumes.

https://doi.org/10.5194/essd-2026-549
Preprint. Discussion started: 10 September 2026

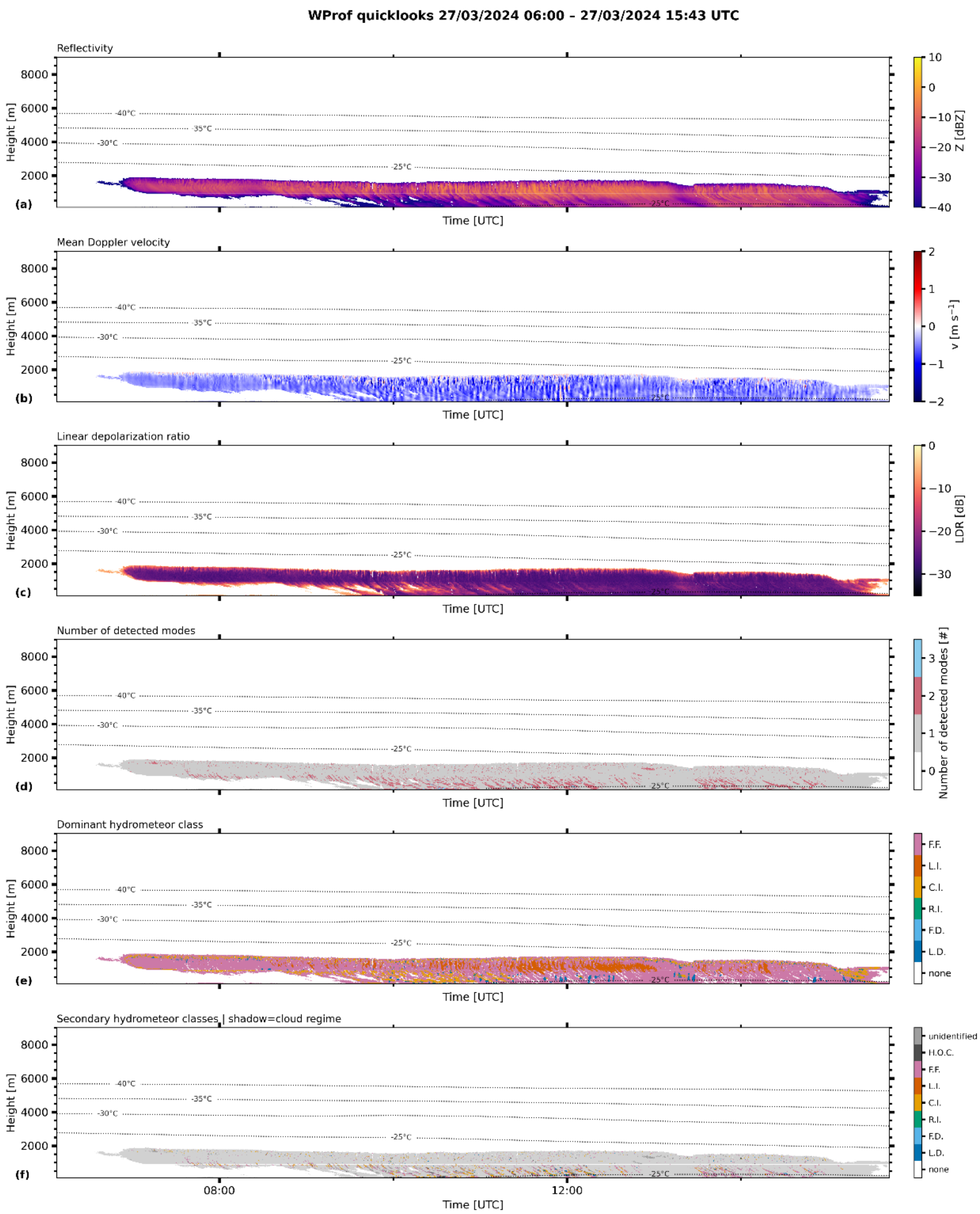

300 **Figure 6: Same as Figure 4 for 27 March 2024 6:00 –15:43 UTC.**

5.4 Case 28–31 March 2024

This case represents a dynamically active, ice-dominated cloud system with strong vertical development and complex microphysics, which gradually evolves into a thinner and more uniform stratiform cloud. The cloud evolution occurs under

https://doi.org/10.5194/essd-2026-549
Preprint. Discussion started: 10 September 2026

three distinct surface pressure regimes. At the beginning of the period, a thin, low-level cloud layer close to the surface is present and gradually dissipates as surface pressure increases, indicating a stabilizing boundary-layer environment. Between 29 March 3:00 and 20:00 UTC, a pronounced pressure drop coincides with an increase in near-surface temperature, consistent with the passage of a warm-air intrusion and enhanced dynamical forcing. During this phase, the cloud system deepens substantially, reaching altitudes of approximately 6–7 km prior to the transition to the final regime. After 29 March 20:00 UTC, surface pressure rises again, marking a more stable post-intrusion regime. During this period, the cloud becomes shallower and more homogeneous, while overlying upper-level cloud layers intermittently provide seeding to lower-level clouds, consistent with a seeding–feeding mechanism that sustains cloudiness near the surface despite an overall weakening of the system (Figure 7).

The LDR is frequently elevated, particularly during and after the deepening phase, indicating the presence of non-spherical ice particles. Figure 4.4 f shows localized occurrences of a secondary Doppler mode, which appears primarily during the initial phase and during cloud deepening, highlighting the coexistence of distinct ice particle populations. At 17:45 UTC on 28 March (Fig. D4), up to three spectral modes are detected below 1 km. A liquid mode is detected near 1 km alongside ice-particle modes, while rimed ice particles occur very close to the surface. The broad and shifted Doppler velocity distributions in the lower cloud are consistent with the influence of turbulent air motions. As the cloud evolves into a more stratiform structure later in the period, fewer Doppler modes are detected, suggesting a transition toward a more uniform particle population.

Figures 7 e and f further indicate that the cloud is predominantly ice-phase, mainly composed of columnar crystals. During the most dynamically active periods, aggregation leads to the formation of larger ice particles, while liquid droplets are detected only intermittently at lower altitudes, primarily after the cloud deepening phase.

We note that, a localized non-meteorological feature was observed approximately from ground level up 2.0 km, but mostly found at 1.8-2.0 km altitude (visible in Fig. F4-7), characterized by positive terminal velocities of about 0.5–1 m s^{-1}. A filtering procedure based on the peakTree mode-selection algorithm was applied to remove this feature from the processed dataset. Consequently, the feature is not identified as a spectral mode in the processed data, although it remains visible in the raw and Level 1 datasets. Figures 7 d–f show the filtered data, whereas the feature can still be observed in the raw and Level 1 data products. The origin of this feature remains unclear, as it was intermittently observed during this event and during the periods 1–5, 8 and 11–13 April 2024.

https://doi.org/10.5194/essd-2026-549
Preprint. Discussion started: 10 September 2026

Open Access Earth System Science Data Discussions

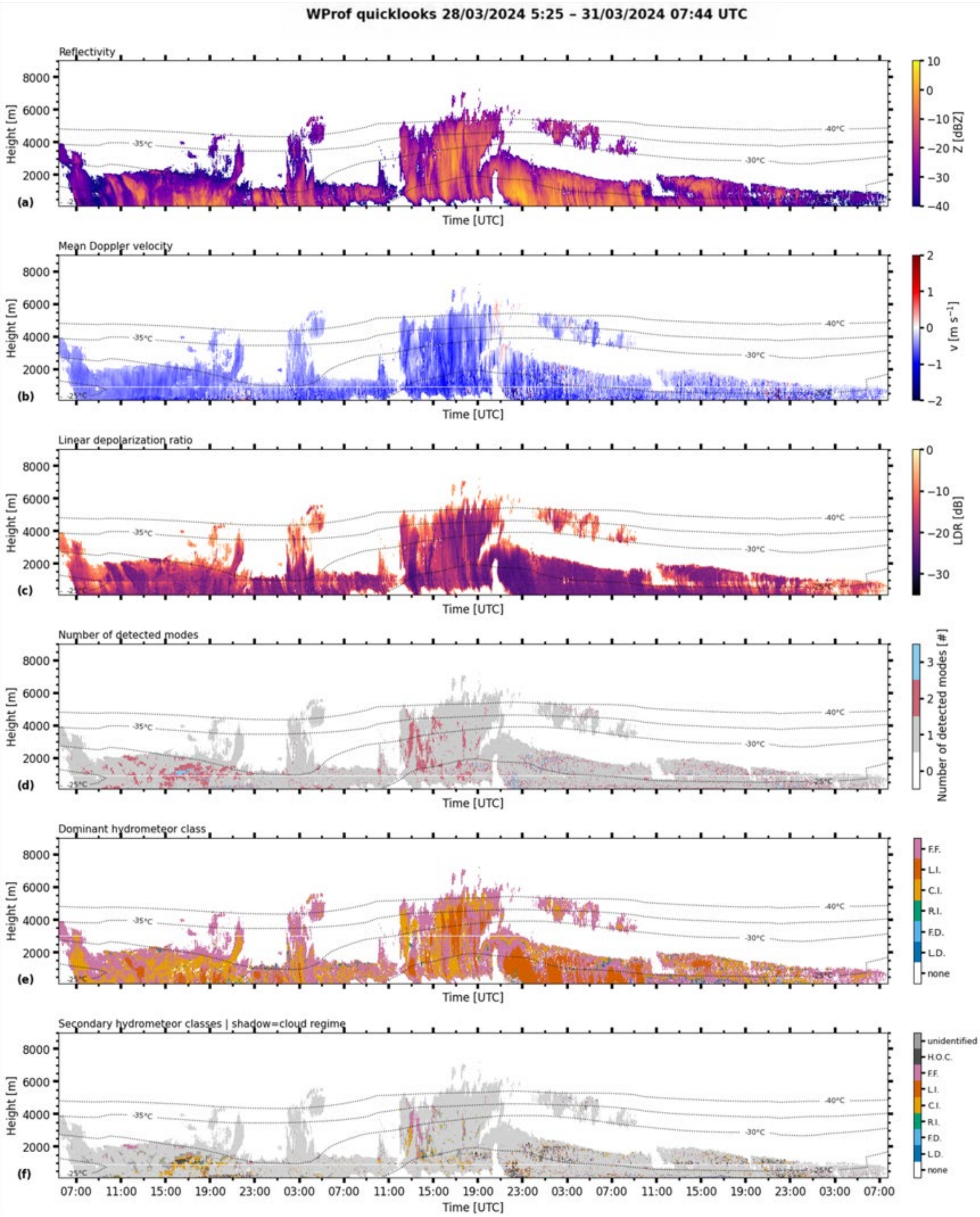

Figure 7: Same as Figure 4 for the period 28 March 2024 5:25 – 31 March 2024 07:44 UTC.

https://doi.org/10.5194/essd-2026-549
Preprint. Discussion started: 10 September 2026

5.5 Case 1–5 April 2024

This case (1–5 April 2024) can be divided into two distinct periods based on the surface meteorological evolution and the corresponding cloud response (Fig. D5). The first period, before 12:00 UTC on 3 April, is characterized by relatively stable surface pressure and near-surface temperature, indicating steady synoptic conditions. The second period, a after 12:00 UTC on 3 April, features a steady increase in surface pressure accompanied by a decrease in near-surface temperature, marking a transition toward a more stable post-forcing regime.

During the first period, a high-level, ice-dominated cloud system persists and gradually descends over time. The cloud exhibits substantial vertical extent, reaching altitudes of approximately7–8 km, and is predominantly characterized by a single mode, alternating between columnar ice crystals and larger aggregates (Figure 8d, e and f). Occasional secondary Doppler modes are also detected, indicating the coexistence of columnar ice and larger aggregated ice particle populations (Figure 8f). The spectrogram at 23:59 UTC on 2 April (Fig. F5) captures this upper cloud and shows that it is composed mainly of columnar ice. This upper cloud may provide ice crystals that seed the lower cloud, although further analysis is needed to confirm this connection. The lower cloud is characterized by a single spectral mode from its top down to approximately 1.5 km, where a liquid mode is detected. Below this level, two distinct spectral modes, interpreted as separate ice populations, extend to the surface. No pronounced spectral broadening is observed at lower levels, suggesting that turbulence is weak.

Toward the end of this first period, the cloud undergoes pronounced deepening, with enhanced reflectivity at lower altitudes, consistent with intensified ice growth and aggregation. During the second period, the cloud rapidly evolves into a shallower, stratiform structure confined closer to the surface. The observations show weaker reflectivity and reduction in vertical extent. The cloud is dominated by larger ice particles, consistent with aggregation, suggesting a transition toward a more homogeneous particle population (Figure 8d-f). This stratiform cloud persists near ground level throughout the remainder of the period, reflecting sustained but weaker ice precipitation under increasingly stable atmospheric conditions.

https://doi.org/10.5194/essd-2026-549
Preprint. Discussion started: 10 September 2026

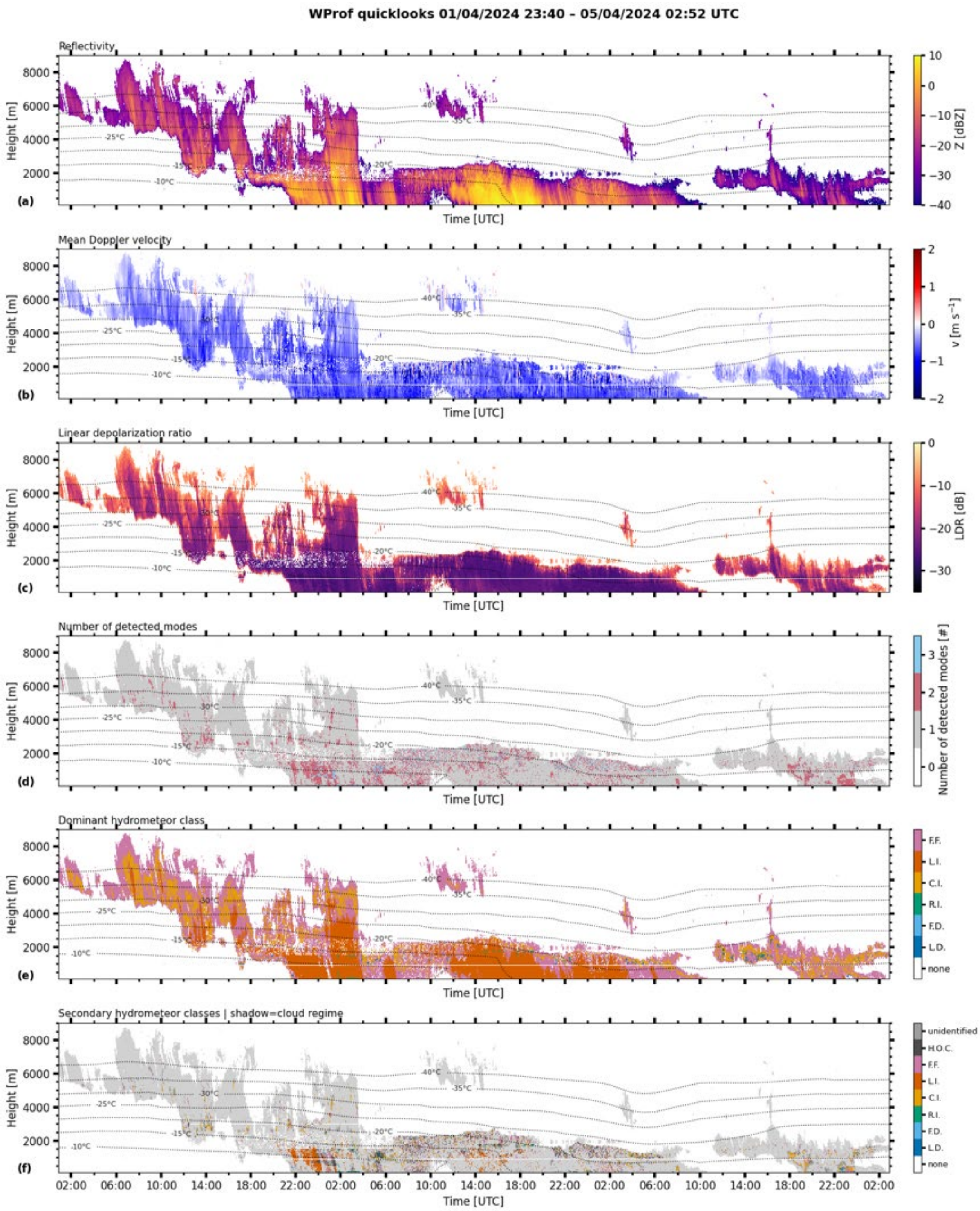

Figure 8: Same as Figure 4 for the period 1 April 2024 23:40 – 5 April 2024 2:52 UTC.

https://doi.org/10.5194/essd-2026-549
Preprint. Discussion started: 10 September 2026

5.6 Case 8 April 2024

This case (8 April 2024) shows a shallow, ice-dominated stratiform cloud layer that formed under steadily increasing surface pressure and gradually rising near-surface temperature (Fig. D6). Overall, the spectrograms (Fig. F6) indicate weak turbulence throughout the cloud lifetime, while precipitation develops following the formation of larger ice particles. At 09:29 UTC (Fig. F6), the cloud extends from near the surface to approximately 2.4 km. Columnar ice is detected in the upper part of the cloud, while fast-falling and large-ice particles become more prominent toward lower levels. Below approximately 800 m, two distinct spectral modes extend to the surface, showing the coexistence of ice-particle populations with different fall velocities. The relatively narrow spectral distributions further support the presence of weak turbulence. Figure 9d indicates the presence of a second Doppler mode, revealing occasional multimodality within the cloud. Figures 9d show that the cloud is mainly composed of ice and dominated by columnar crystals. The occurrence of larger, faster-falling particles is consistent with aggregation and the subsequent development of precipitation.

https://doi.org/10.5194/essd-2026-549
Preprint. Discussion started: 10 September 2026

Open Access Earth System Science Data Discussions

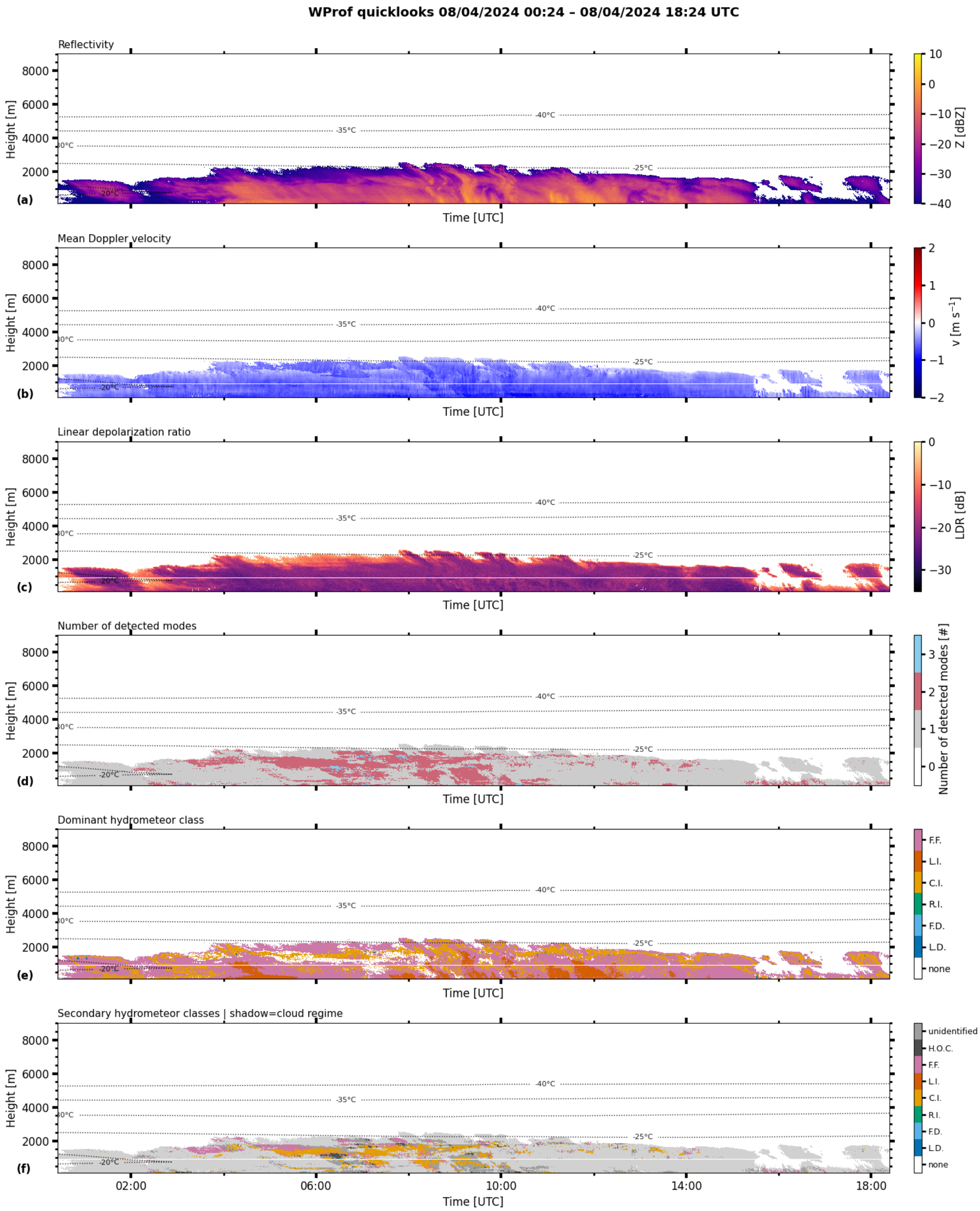

370 **Figure 9: Same as Figure 4 for the period 8 April 2024 0:24 – 18:24 UTC.**

https://doi.org/10.5194/essd-2026-549
Preprint. Discussion started: 10 September 2026

Open Access Earth System Science Data Discussions

5.7 Case 11–13 April 2024

This case (12–13 April 2024) can be divided into two phases based on the surface pressure evolution. Before the pressure increases at 19:00 UTC on 11 April, surface pressure remains relatively low and variable, while near-surface temperature fluctuates around −25 °C. After 19:00 UTC on 11 April, surface pressure rises steadily, accompanied by a gradual increase in near-surface temperature (Fig. D7).

During the first phase, a seeder–feeder cloud configuration is observed. An upper-level seeder cloud, located between approximately 3 and 7 km, produces ice particles that fall into a lower-level feeder cloud extending up to ~2–3 km. This seeding–feeding interaction contributes to the formation of a secondary Doppler mode within the lower cloud and, intermittently, a third mode within the precipitation curtain below. Enhanced radar reflectivity and more negative Doppler velocities beneath the seeder cloud indicate intensified precipitation associated with the interaction between the two cloud layers (Figure 10). The spectrogram at 09:57 UTC on 11 April (Fig. F7) illustrates this structure. The upper cloud extends from approximately 3 to 6.8 km and contains mainly columnar ice and a fastest-falling population. As the particles descend, radar reflectivity increases and Doppler velocities become more negative, while large ice particles become more prominent within the lower cloud, while below approximately 700 m, a second modes extend to the surface.

During the second phase, the cloud becomes shallower and more stratiform, precipitation weakens, and Doppler spectral complexity decreases, indicating a transition toward a more uniform microphysical regime, dominated by aggregated ice particles with occasional coexistence of supercooled liquid droplets (Figure 10f). Figures 10e and f further show showers of columnar ice crystals and large aggregated ice particles descending through the cloud, particularly during the most dynamically active phase. Sporadic liquid droplets were also detected together with rimed ice (Figure 10e and f), primarily within the lower cloud layer and during periods of enhanced precipitation.

https://doi.org/10.5194/essd-2026-549
Preprint. Discussion started: 10 September 2026

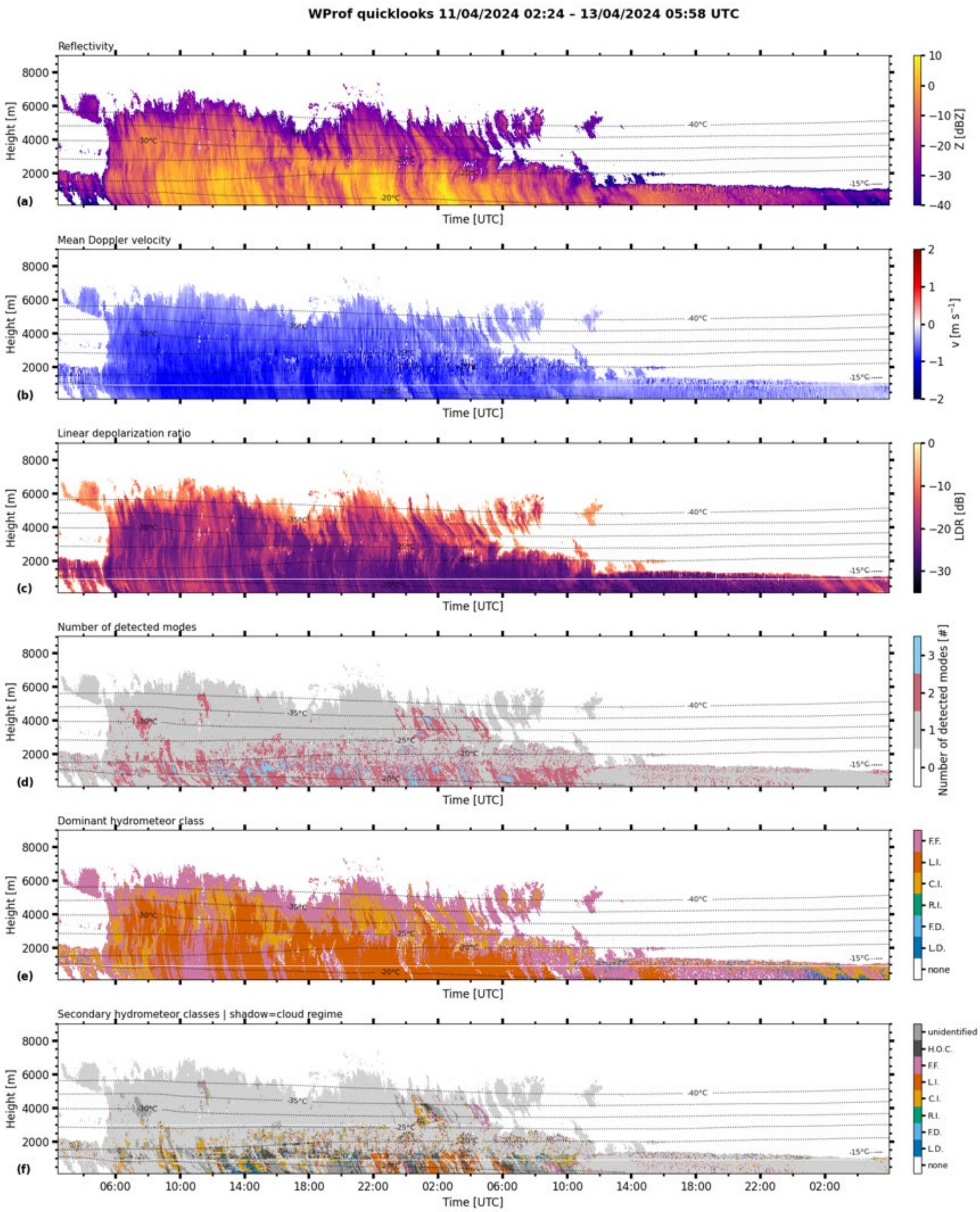

Figure 10: Same as Figure 4 for the period 11 April 2024, 2:24 UTC to 13 April 2024, 5:58 UTC.

https://doi.org/10.5194/essd-2026-549
Preprint. Discussion started: 10 September 2026

Conclusions

In this paper, we present a set of 94-GHz spectral radar data collected over VRS. The dataset includes peak-resolved Doppler spectral products derived using the peakTree algorithm, combined with hydrometeor classification schemes implemented within pyLARDA. This combined framework enables the systematic identification of coexisting Doppler spectral modes and their association with distinct hydrometeor populations, providing a more physically detailed representation of cloud microstructure compared to conventional moment-based radar products.

The dataset captures a wide range of Arctic cloud regimes and microphysical processes evolving under different synoptic conditions, including warm-air intrusions and pronounced changes in surface pressure (Cases 1, 3, 4, 6, and 7). In several cases, cloud systems evolved from elevated ice clouds into vertically deep, precipitating structures during periods of enhanced dynamical forcing, before transitioning into shallower, more stratiform clouds as atmospheric conditions became increasingly stable (Cases 1, 4, 5, and 7). Ice-phase processes dominated throughout all events, with columnar ice crystals prevailing during the early and more dynamically active stages, while aggregation into larger ice particles became increasingly important during cloud deepening and precipitation (Cases 1, 4, 5, and 7).

The findings are broadly consistent with previous Arctic cloud observations, the peak-resolved spectral analysis shows that multimodal Doppler structures are consistent with similar observations reported in previous studies (e.g. Luke et al., 2010; Verlinde et al., 2013) Doppler spectra were generally characterized by a single dominant mode, although intermittent multimodality was observed during periods of active growth, seeder–feeder interactions, or enhanced turbulence. This demonstrates that the coexistence of multiple hydrometeor populations within a single radar volume is a common feature of Arctic cloud systems rather than an exception.

Some events showed signatures consistent with the presence of supercooled liquid water layers, particularly near cloud tops or within low-level residual clouds; however, liquid occurrence was typically sporadic and short-lived (Cases 2, 3, 4, 5, and 7). Even though supercooled liquid layers are often thin and short-lived, they play a disproportionate role in the Arctic radiative budget, as liquid droplets are highly efficient emitters of longwave radiation. As a result, small changes in the relative amounts of liquid and ice can lead to significant differences in surface energy fluxes.

Overall, the dataset illustrates that multimodality is a common feature of Arctic cloud systems above VRS, especially during periods of active growth, aggregation, or vertical layer interaction. At the same time, the transition toward more homogeneous, single-mode spectra during stable conditions suggests that spectral complexity can serve as an indicator of cloud dynamical state and microphysical activity. The observations presented here therefore provide valuable constraints for improving microphysical parameterizations and for evaluating radar forward simulators that aim to reproduce Doppler spectral signatures.

Finally, the CLAVIER dataset offers significant potential for future research, including process-level studies of aerosol–cloud interactions, investigation of precipitation formation pathways, and evaluation of cloud phase partitioning in numerical weather prediction and climate models. The combination of peak-resolved Doppler spectra with auxiliary meteorological and aerosol

https://doi.org/10.5194/essd-2026-549
Preprint. Discussion started: 10 September 2026

Open Access Earth System Science Data Discussions

observations further enables synergistic analyses aimed at improving the representation of Arctic clouds and their radiative effects in a changing climate.

Appendix A. Summary of variables in the WProf dataset

The WProf dataset includes the following radar variables for all available profiles: Equivalent reflectivity factor (Ze), identified in the data files by the short name Ze, Signal-to-noise ratio (SNR), identified by SnR, Mean Doppler radial velocity, identified by Mean-velocity, Spectral width, identified by Spectral-width, Spectral skewness, identified by Spectral-skewness, Spectral kurtosis, identified by Spectral-kurtosis, Noise level at each range gate, identified by Noise_level, Noise floor at each range gate, identified by Noise_floor.

Integrated water vapor, identified by Integrated-water-vapor, and liquid water path (LWP), identified by Liquid-water-path, are included in the data files. However, the passive microwave radiometer providing the native LWP retrievals was not radiometrically calibrated during the campaign. Consequently, the original LWP retrievals should be considered preliminary and are not recommended for quantitative analyses without further calibration. To provide an improved estimate of LWP, the microwave brightness temperatures were radiometrically calibrated using forward simulations constrained by the available radiosonde profiles Dorff et al. (2026), following the methodology of Billault-Roux & Berne (2021). The resulting pyLWP retrievals are provided in separate NetCDF files. Although these calibrated retrievals substantially improve the consistency of the observations, they should still be regarded as indicative of LWP variability, and quantitative analyses should be interpreted with appropriate caution.

The Doppler spectra are stored separately in dedicated files containing the following variables: Spectral reflectivity for chirp 0, corresponding to the lowest part of the profile (Table 1), identified by Doppler-spectrum-vert-chirp0; Spectral reflectivity for chirp 1, corresponding to the middle part of the profile, identified by Doppler-spectrum-vert-chirp1; Spectral reflectivity for chirp 2, corresponding to the upper part of the profile, identified by Doppler-spectrum-vert-chirp2.

The following atmospheric variables measured by the automated weather station integrated into the radar system are included in both radar moment and spectral data files: Atmospheric pressure, identified by Barometric-pressure; Air temperature, identified by Environment-temp; Relative humidity with respect to liquid water, identified by Rel-humidity; Horizontal wind direction, identified by Wind-direction; Horizontal wind speed, identified by Wind-speed.

Appendix B. Spectral Postprocessing Procedure

Spectral peak detection was performed independently for each radar chirp using chirp-specific temporal averaging, spectral smoothing, noise estimation, and detection parameters. Temporal averaging windows of 9 s and 5 s were only applied to chirps 0 and 1, respectively. Doppler spectra were first smoothed and then filtered using noise-based thresholds. For all chirps, smoothing was implemented using a second-order Savitzky–Golay polynomial filter. Spectral peaks were searched within Doppler velocity intervals of 0.23 m s^{-1} for chirps 0 and 1 and 0.30 m s^{-1} for chirp 2.

Noise levels were estimated separately for each chirp using a consistent, spectrum-based approach. For each chirp (0, 1, and 2), Doppler spectra were first averaged over the selected time and range windows and pre-processed to suppress narrow, non-

https://doi.org/10.5194/essd-2026-549
Preprint. Discussion started: 10 September 2026

physical spectral artefacts. Noise statistics were then derived directly from the cleaned co-polarized Doppler spectrum by selecting the 100 smallest non-zero, finite spectral values, which were assumed to represent noise-dominated bins. The mean of this subset was taken as the noise level, while its standard deviation quantified noise variability. A conservative detection threshold was subsequently defined as the noise level plus 18 times the standard deviation, providing robust suppression of residual noise fluctuations. This scalar threshold was applied uniformly across the Doppler velocity axis for peak detection in the co-polarized channel.

For the cross-polarized channel, the noise threshold was defined independently using the pre-computed noise level, derived from the summed horizontal and vertical receiver noise powers and corrected for the effective number of spectral averages per chirp. This noise level was averaged over the selected time–range window and applied directly as the detection threshold.

Then, the LDR was computed as the ratio of cross- to co-polarized spectral power. Spectral bins were masked if either polarization channel fell below its respective noise threshold, or if the cross-polarized signal did not exceed the instrumental decoupling limit relative to the co-polarized signal, ensuring physically meaningful LDR estimates. Finally, the spectral peaks were retained if their prominence exceeded 0.8 dB for chirps 0 and 1 and 0.5 dB for chirp 2, while no minimum peak width constraint was imposed, and up to 15 spectral modes were allowed per time–range gate.

Appendix C. Hydrometeor classification scheme

The hydrometeor classification scheme was developed to identify persistent stratiform, supercooled cloud layers, with a focus on long-lived systems relevant for Doppler spectral analysis. This filtering is implemented within the pyLARDA framework Bühl et al., 2021), which provides access to raw Doppler spectra and enables peak-resolved analysis. The selection algorithm is adapted from (Bühl et al., 2016), allowing for the automated preselection of cloud structures suitable for multimodal Doppler spectral interpretation. Hydrometeor typing is performed using a rule-based decision tree applied to peakTree-resolved Doppler spectra. For each radar resolution volume, individual spectral peaks (Modes) are identified and characterized by their Ze_m, v_m, spectral prominence, and LDR_m. Hydrometeor classes are then assigned by applying physically motivated, heuristic threshold criteria to these node properties, following established interpretations of cloud radar Doppler and polarimetric signatures. Liquid cloud droplets are identified by low reflectivity and near-zero Doppler velocity, consistent with small droplets whose motion is dominated by turbulence rather than gravitational settling. Modes are classified as:

- Liquid if $Ze_m < -20$ dBZ and $|v| < 0.3$ m s^{-1}, with an additional constraint of low depolarization ($LDR_m < -20$ dB) to restrict the selection to spherical particles. These criteria are consistent with Doppler cloud radar observations of supercooled liquid layers in Arctic mixed-phase clouds and with velocity-based liquid–ice separation approaches (Shupe et al., 2006; Luke et al., 2010; Oue et al., 2018).
- Frozen drops and other dense, compact ice particles are identified by the presence of fast-falling, well-separated Doppler spectral peaks. Modes are classified as frozen drops when their mean Doppler velocity exceeds a magnitude of 1.8 m s^{-1} downward ($v_m < -1.8$ m s^{-1}) and their spectral prominence exceeds 2 dB, ensuring robust separation from weaker spectral modes.

https://doi.org/10.5194/essd-2026-549
Preprint. Discussion started: 10 September 2026

- Rimed ice particles are detected based on the coexistence of multiple spectral peaks with substantially different fall velocities within the same radar volume. Riming is inferred when the absolute velocity separation between the slowest and fastest modes exceeds 1.5 m s^{-1}, indicating the simultaneous presence of unrimed cloud ice and more heavily rimed or aggregated particles. This criterion follows the interpretation of bimodal Doppler spectra associated with riming processes and is consistent with peakTree-based multimodal analyses (Kalesse et al., 2016; Radenz et al., 2019).
- Columnar ice crystals are selected using a combination of moderate reflectivity and elevated LDR_m values, reflecting the nonspherical geometry and preferential orientation of needle-like or columnar habits. Modes are classified as columnar ice when $Ze_m < -10$ dBZ and -20 dB $\leq LDR_m \leq -15$ dB.
- Large ice particles are further distinguished by relatively high reflectivity combined with low depolarization, consistent with aggregates or compact snow particles with reduced sphericity compared to pristine crystals. Modes are classified as large ice when $Ze_m \geq -10$ dBZ and $LDR_m < -20$ dB.
- Fastest-falling mode selector was applied to identify the spectral peak with the maximum downward Doppler velocity within each radar volume. This selector does not impose explicit thresholds on reflectivity or depolarization and serves as a generic proxy for the largest or densest hydrometeors present.

The classes along the criterion are summarized in Table A1.

Hydrometeor class	**Physical interpretation**	**Reflectivity (Ze_m)**	**Doppler velocity (v_m)**	**LDRm**	**Additional criteria**
Liquid droplets	Small supercooled cloud droplets dominated by turbulence	Zem < −20 dBZ	|vm| < 0.3 m s^{-1}	LDRm < −20 dB	Near-zero fall velocity; spherical particles
Frozen drops	Dense, compact ice particles with rapid gravitational settling	–	vm < −1.8 m s^{-1}	–	Spectral prominence > 2 dB
Rimed ice	Coexistence of unrimed ice and heavily rimed or aggregated particles	–	–	–	Velocity separation between slowest and fastest modes > 1.5 m s^{-1}
Columnar ice	Needle-like or columnar ice crystals with preferred orientation	Zem < −10 dBZ	–	−20 dB ≤ LDRm ≤ −15 dB	Enhanced depolarization due to nonspherical shape

https://doi.org/10.5194/essd-2026-549
Preprint. Discussion started: 10 September 2026

Hydrometeor class	Physical interpretation	Reflectivity (Ze_m)	Doppler velocity (v_m)	LDRm	Additional criteria
Large ice	Aggregates or compact snow particles	Zem ≥ −10 dBZ	–	LDRm < −20 dB	Higher reflectivity with weak depolarization
Fastest-falling mode	Proxy for largest or densest hydrometeors	–	Minimum (most negative) vm	–	No explicit Zem or LDRm thresholds

Table A 1. Hydrometeor classification scheme based on Doppler-spectral node properties derived from W-band cloud radar observations.

Appendix D. Meteograms per case

The following meteograms summarize the near-surface meteorological conditions during each case. They combine air temperature, surface pressure, and relative humidity from the Vaisala WXT536 with wind measurements from the 9 m climate mast. Relative humidity with respect to ice was calculated using Murray (1967), and all times are reported in UTC.

Case 23-25 March 2024

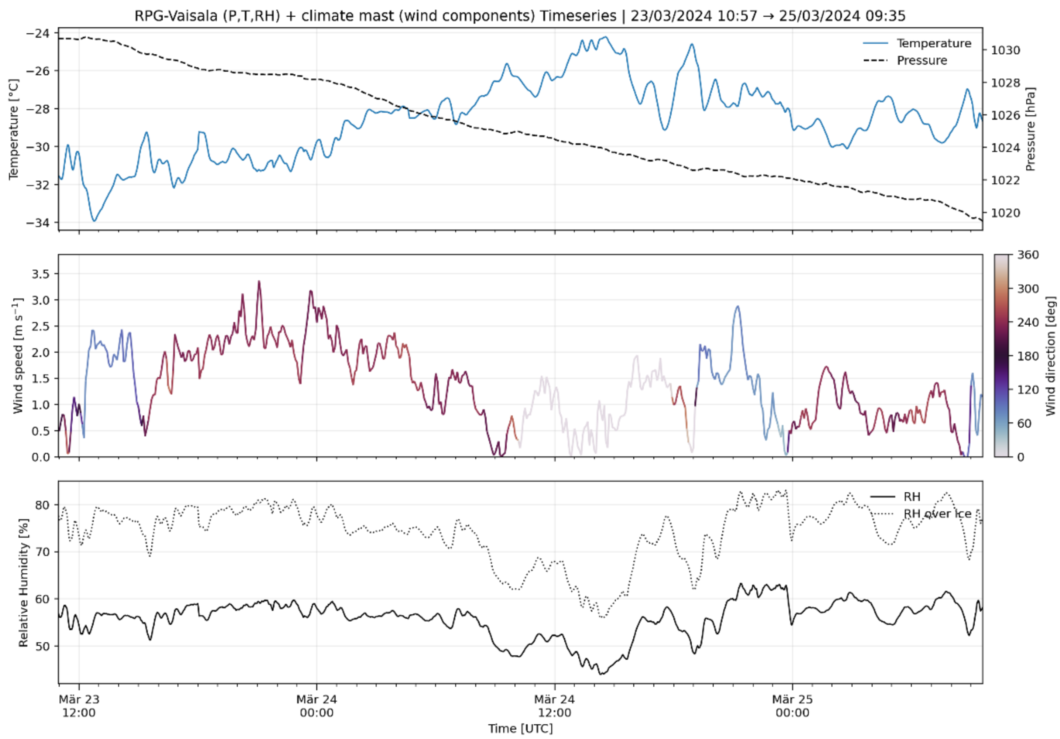

Figure D1. Time series of near-surface wind measurements at the 9 m climate together with the ground measurements of Temperature, Relative humidity and pressure obtained from the Vaisala compact weather station mounted at WProf for the case

https://doi.org/10.5194/essd-2026-549
Preprint. Discussion started: 10 September 2026

23–25 March 2024 (UTC). a) The air temperature (solid blue line) and surface pressure (black dashed line). b) The wind speed, while line colour indicates the wind direction. c) The relative humidity with respect to water (solid line) and relative humidity with respect to ice (dashed line).

Case 25-26 March 2024

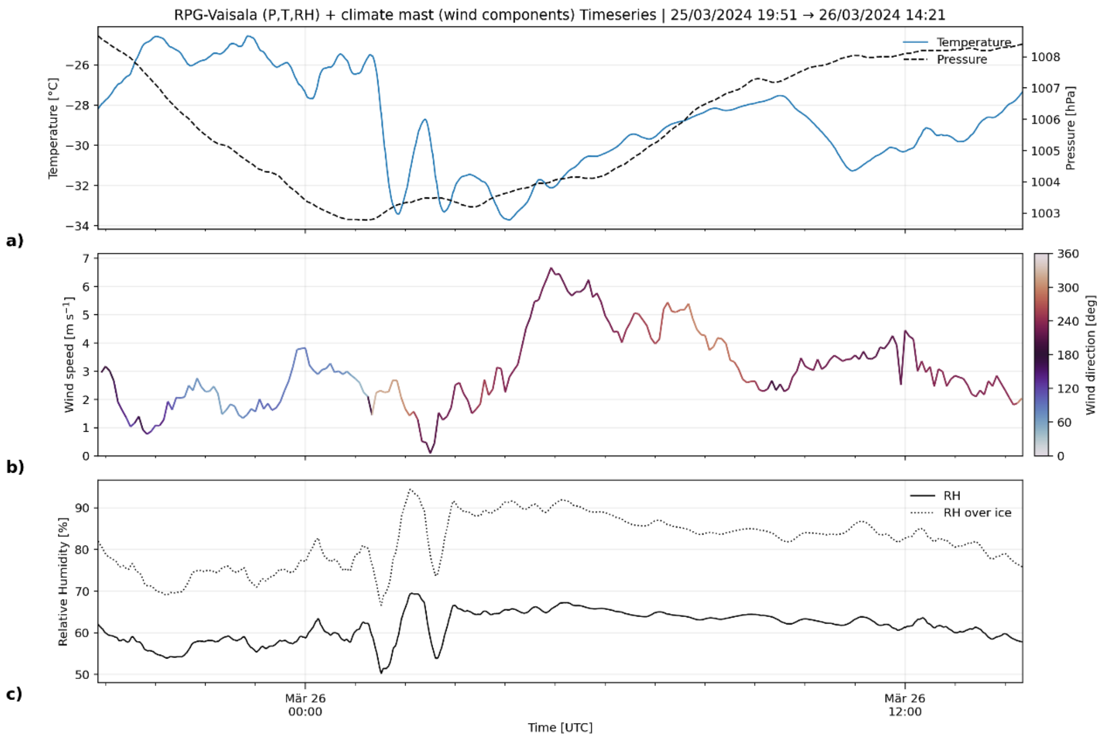

Figure D2. Same as Fig. D1 for the case 25–26 March 2024 (UTC).

https://doi.org/10.5194/essd-2026-549
Preprint. Discussion started: 10 September 2026

Open Access Earth System Science Data Discussions

Case 27 March 2024

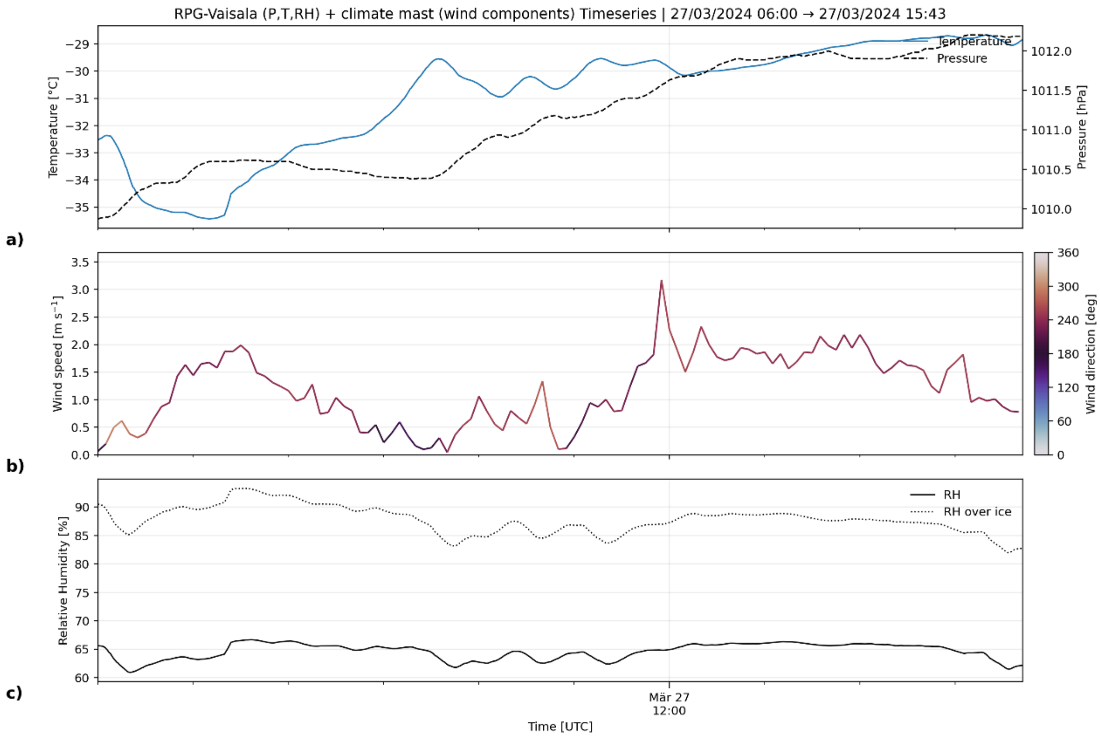

Figure D3. Same as Fig. D1 for the period 27 March 2024 (UTC).

https://doi.org/10.5194/essd-2026-549
Preprint. Discussion started: 10 September 2026

Open Access Earth System Science Data Discussions

Case 28-31 March 2024

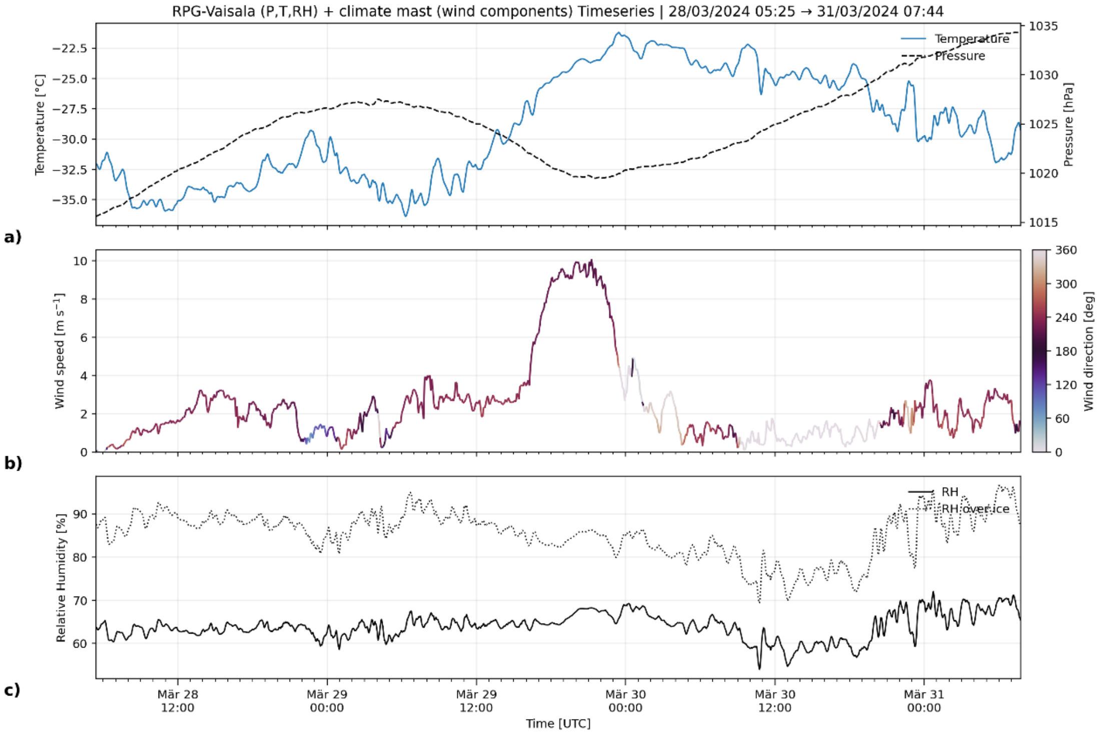

Figure D4. Same as Fig. D1 for the case 28–31 March 2024 (UTC).

https://doi.org/10.5194/essd-2026-549
Preprint. Discussion started: 10 September 2026

Case 1-5 April 2024

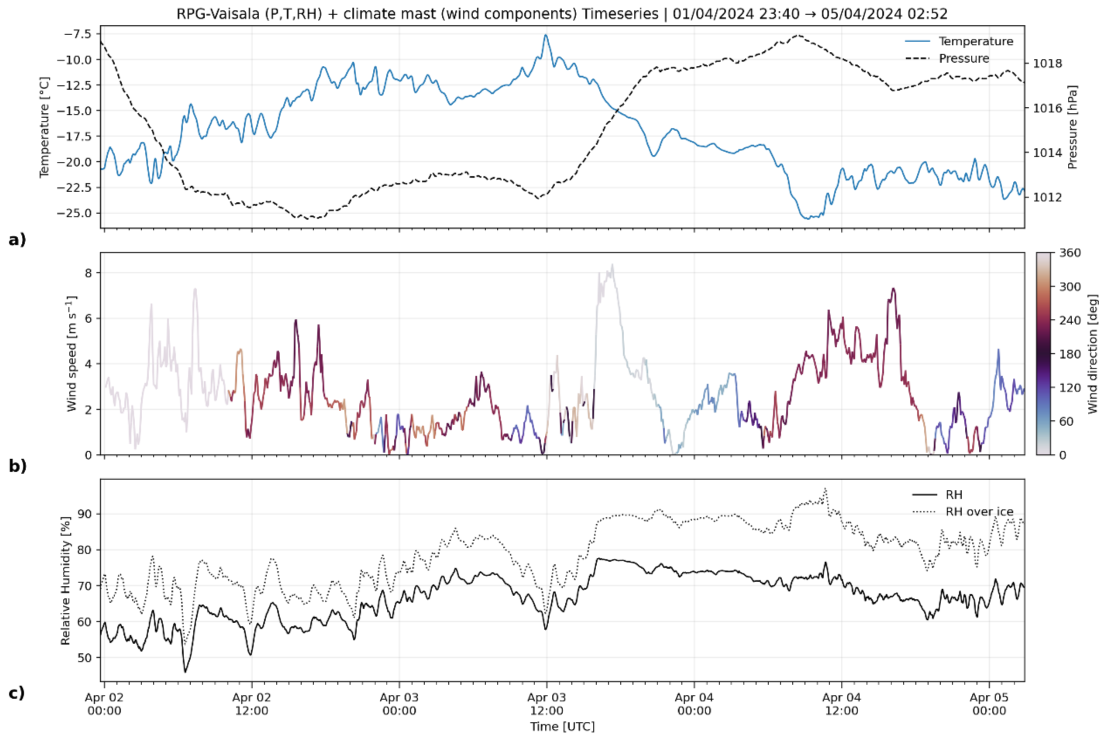

Figure D5. Same as Fig. D1 for the case 1–5 April 2024 (UTC).

https://doi.org/10.5194/essd-2026-549
Preprint. Discussion started: 10 September 2026

Case 8 April 2024

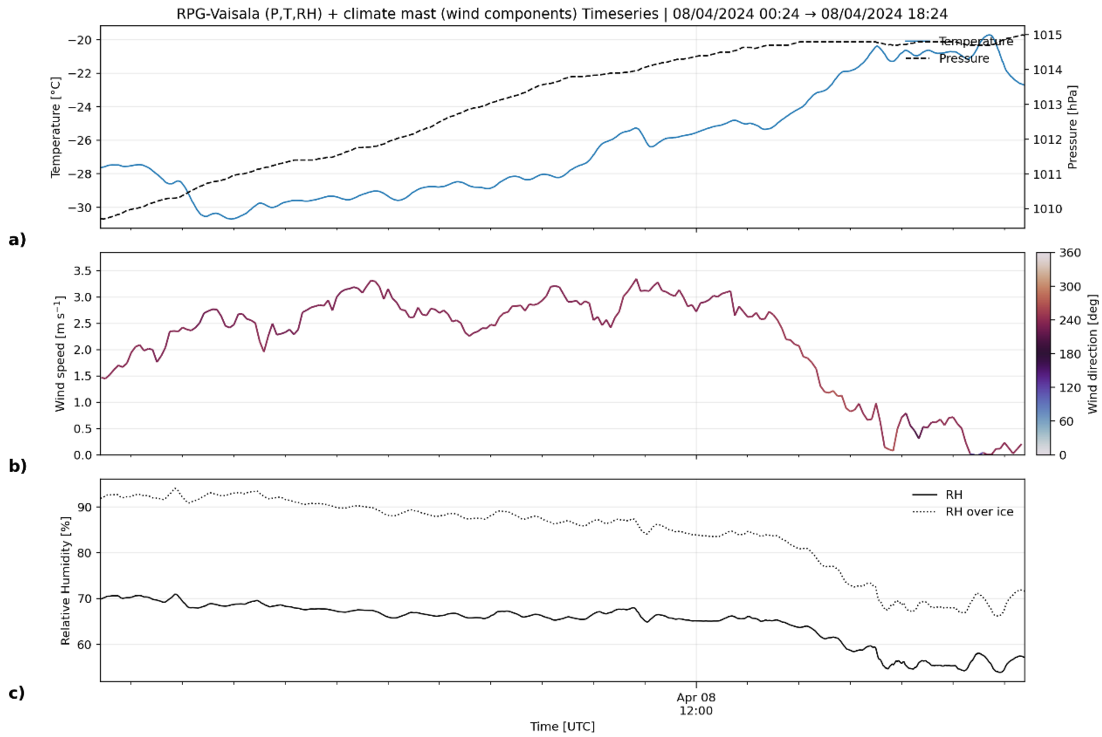

535 **Figure D6. Same as Fig. D1 for the case 8 April 2024 (UTC).**

https://doi.org/10.5194/essd-2026-549
Preprint. Discussion started: 10 September 2026

Case 11-13 April 2024

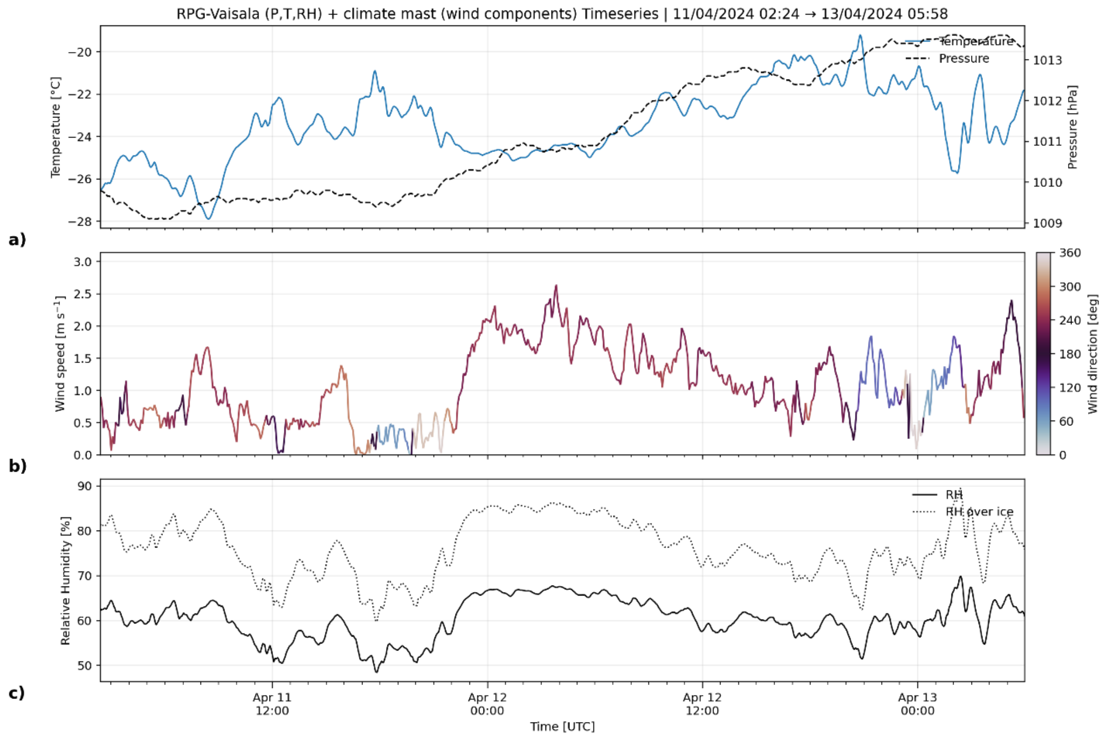

Figure D7. Same as Fig. D1 for the case 11–13 April 2024 (UTC).

Appendix E. Mode Resolved Spectral Datasets

The mode-resolved spectral datasets provide a detailed representation of the multimodal Doppler structure of Arctic cloud systems observed during the CLAVIER campaign. For each selected case, time–height cross sections of peakTree-resolved spectral properties are presented separately for individual Doppler modes, including equivalent reflectivity, mean Doppler velocity, linear depolarization ratio, and the temporal variability of Doppler velocity. The dominant mode (Mode 0) captures the bulk cloud and precipitation signal, while higher-order modes represent weaker, intermittently detected hydrometeor populations with distinct fall speeds and polarimetric signatures. Additionally, the boxplot distributions summarize the statistical characteristics of radar observables for each spectral mode, highlighting systematic differences between dominant and secondary modes and illustrating the added information provided by peak-resolved Doppler spectral analysis.

https://doi.org/10.5194/essd-2026-549
Preprint. Discussion started: 10 September 2026

Open Access Earth System Science Data Discussions

Case 23-25 March 2024

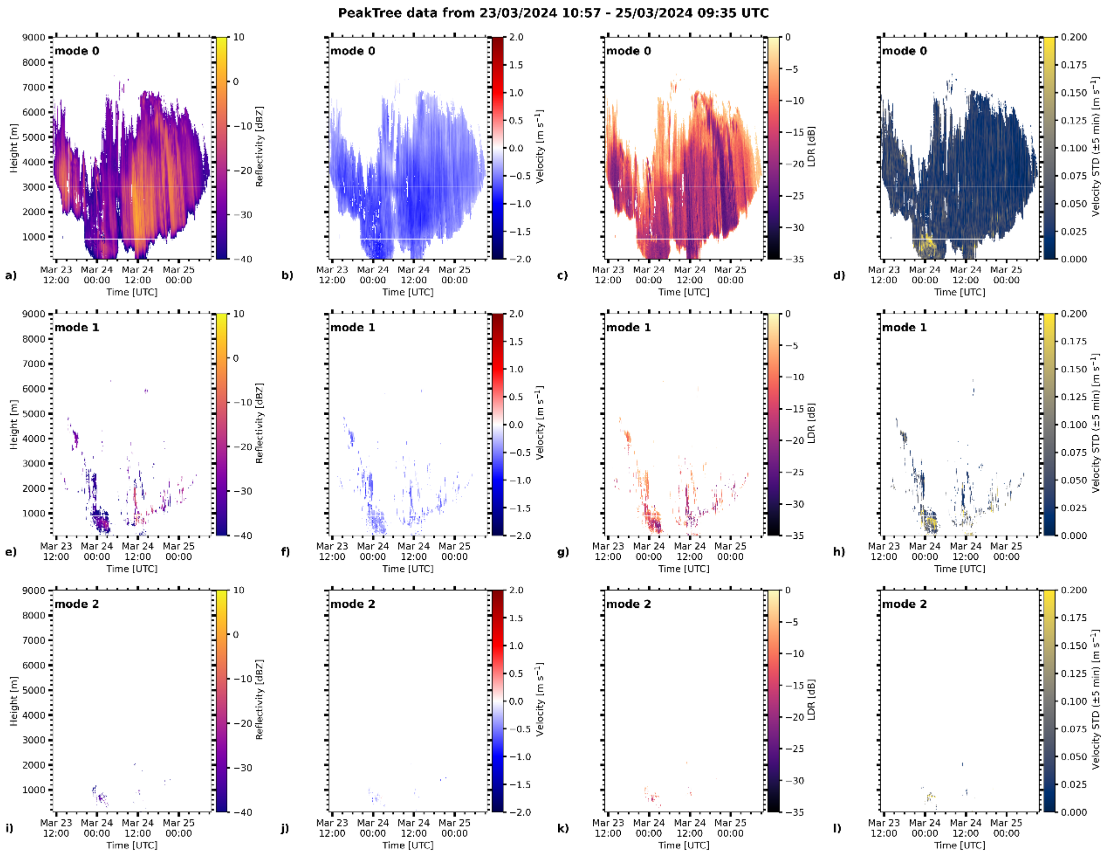

Figure E1. Time–height cross sections of PeakTree-resolved Doppler spectral properties derived from WProf radar observations for the period 23 March 2024 10:57 – 25 March 2024 9:35 UTC. Rows correspond to individual spectral modes (modes 0–2), while columns show (from left to right) the Z, v, LDR, and the temporal standard deviation of Doppler velocity computed over a ±5 min window. Mode 0 represents the dominant spectral peak and captures the bulk cloud structure, whereas higher-order modes (modes 1 and 2) highlight weaker, intermittently detected secondary hydrometeor populations with distinct fall speeds and polarimetric signatures. This representation illustrates the multimodal Doppler spectral structure and its evolution within the observed cloud system.

https://doi.org/10.5194/essd-2026-549
Preprint. Discussion started: 10 September 2026

Open Access Earth System Science Data Discussions

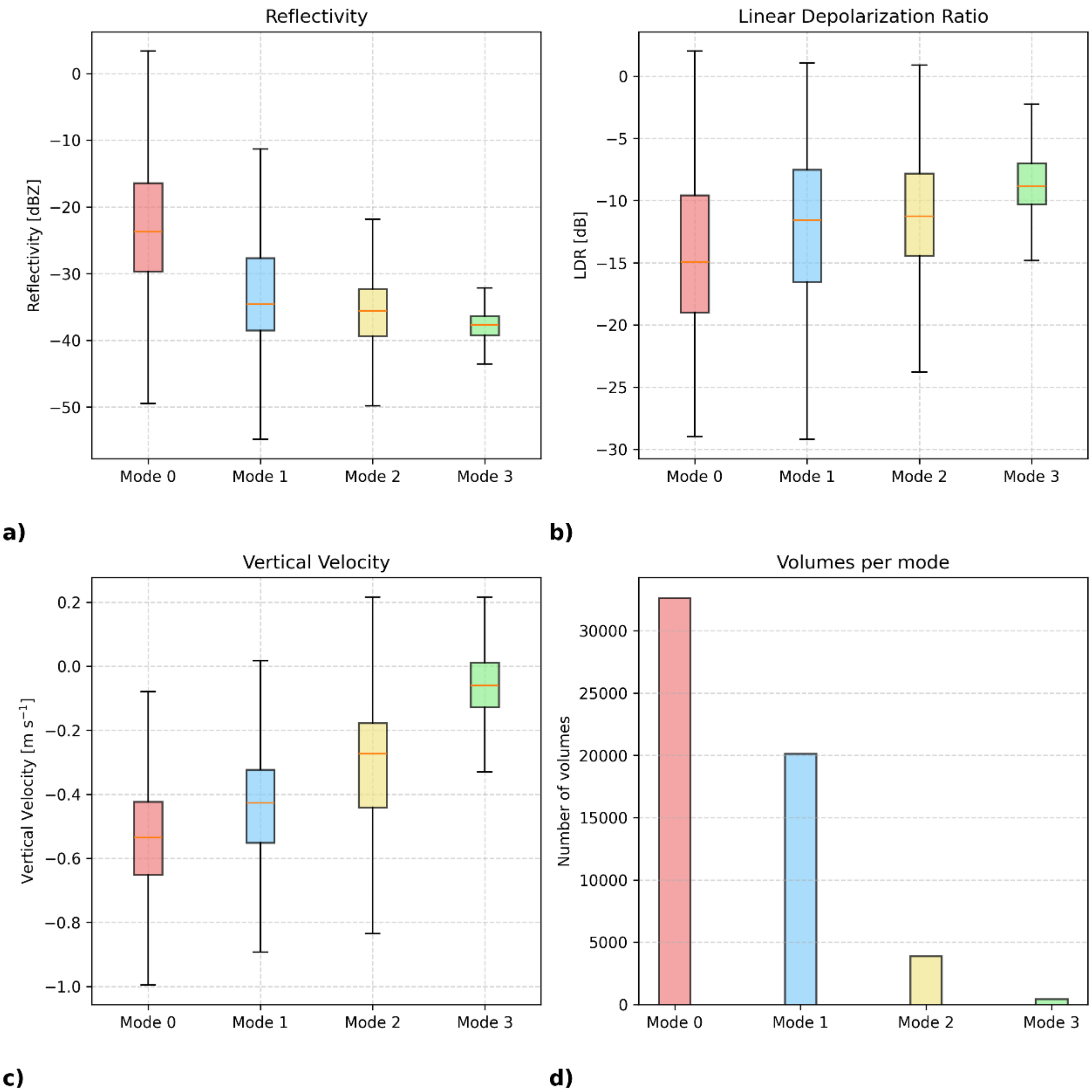

Figure E2. Boxplot distributions of radar observables for peak-resolved Doppler spectral modes (Modes 0–3) for the period 23 March 2024 10:57 – 25 March 2024 9:35 UTC. a) The equivalent reflectivity, b) linear depolarization ratio, c) mean vertical Doppler velocity and d) the number of the observed volumes. Each box represents the interquartile range with the median indicated by the horizontal line, while whiskers denote the data spread excluding outliers. The progression from Mode 0 to Mode 3 highlights systematic shifts toward lower reflectivity, higher (less negative) LDR, and reduced fall velocities, consistent with a transition from faster-falling, more irregular ice particles to weaker, slower-falling hydrometeor populations.

https://doi.org/10.5194/essd-2026-549
Preprint. Discussion started: 10 September 2026

Case 25-26 March 2024

565

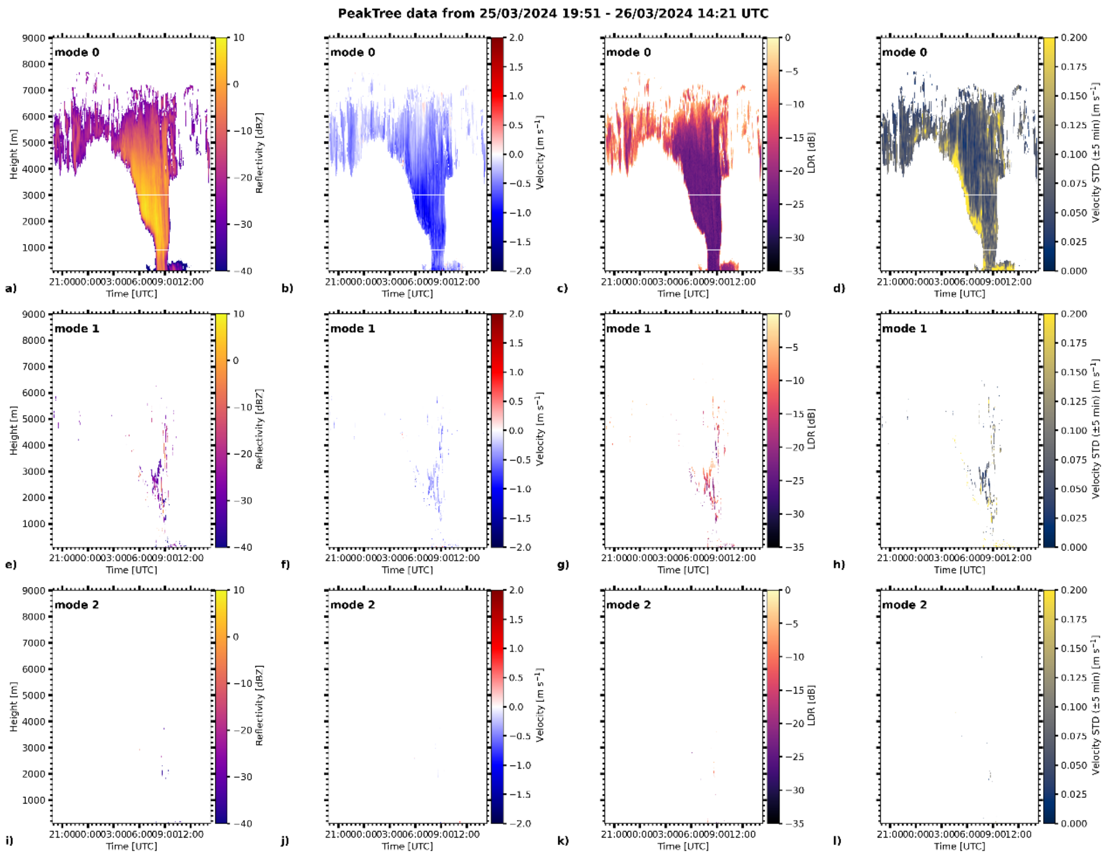

Figure E3. Same as Fig. E1 for the period 25 March 2024 19:51 – 26 March 2024 14:21 UTC.

https://doi.org/10.5194/essd-2026-549
Preprint. Discussion started: 10 September 2026

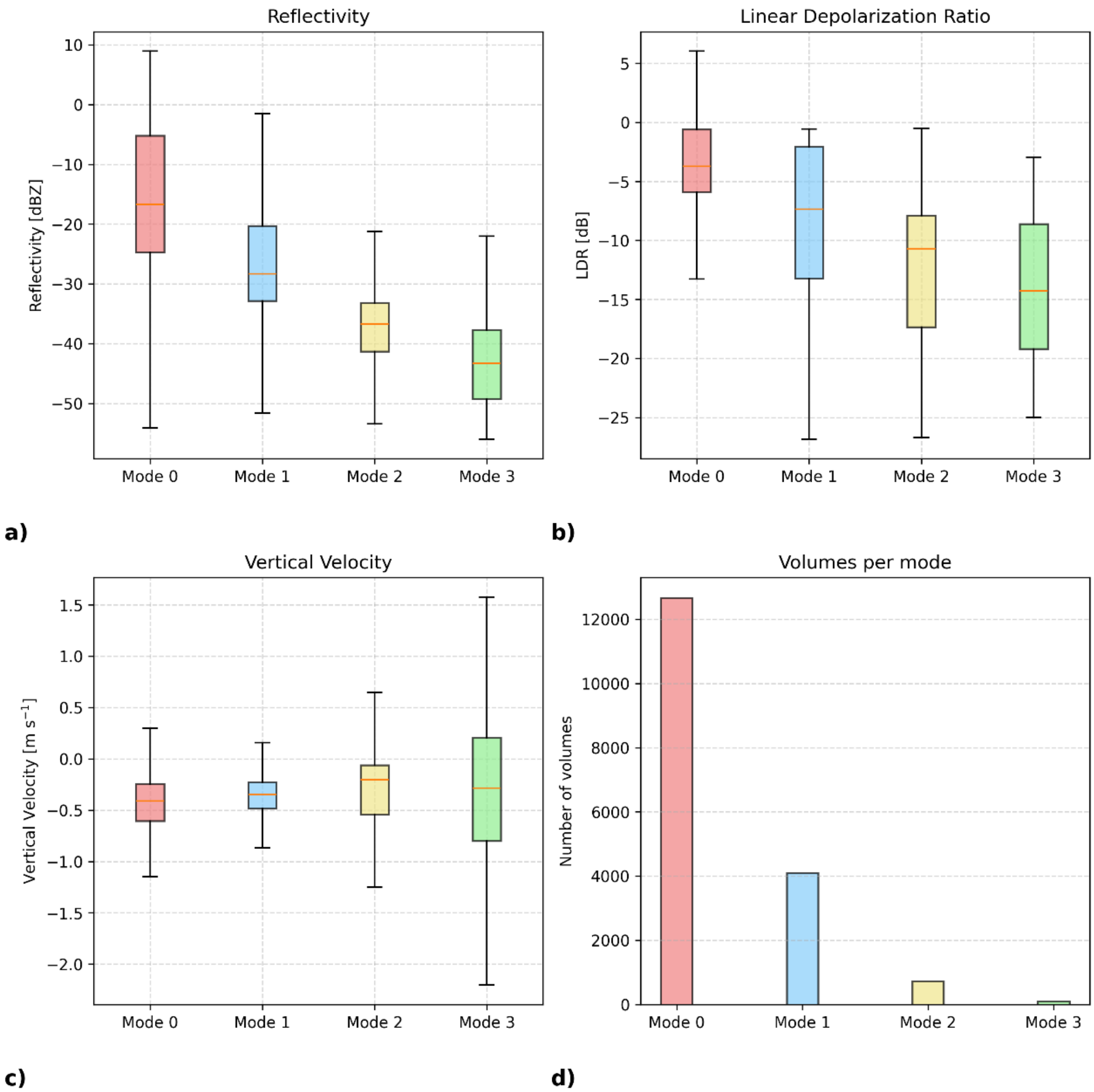

Figure E4. Same as Fig. E2 for the period 25 March 2024 19:51 – 26 March 2024 14:21 UTC.

https://doi.org/10.5194/essd-2026-549
Preprint. Discussion started: 10 September 2026

Case 27 March 2024

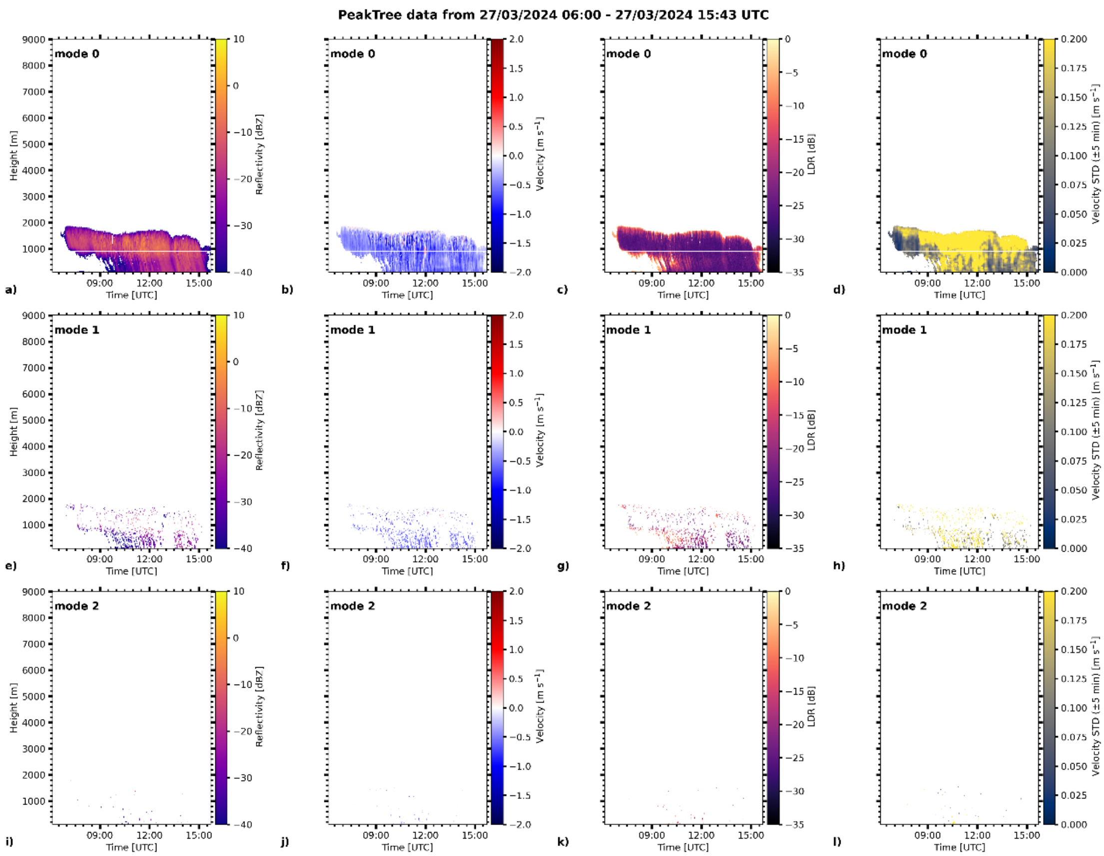

Figure E5. Same as Fig. E1 for the period 27 March 2024 6:00 –15:43 UTC.

https://doi.org/10.5194/essd-2026-549
Preprint. Discussion started: 10 September 2026

Open Access Earth System Science Data Discussions

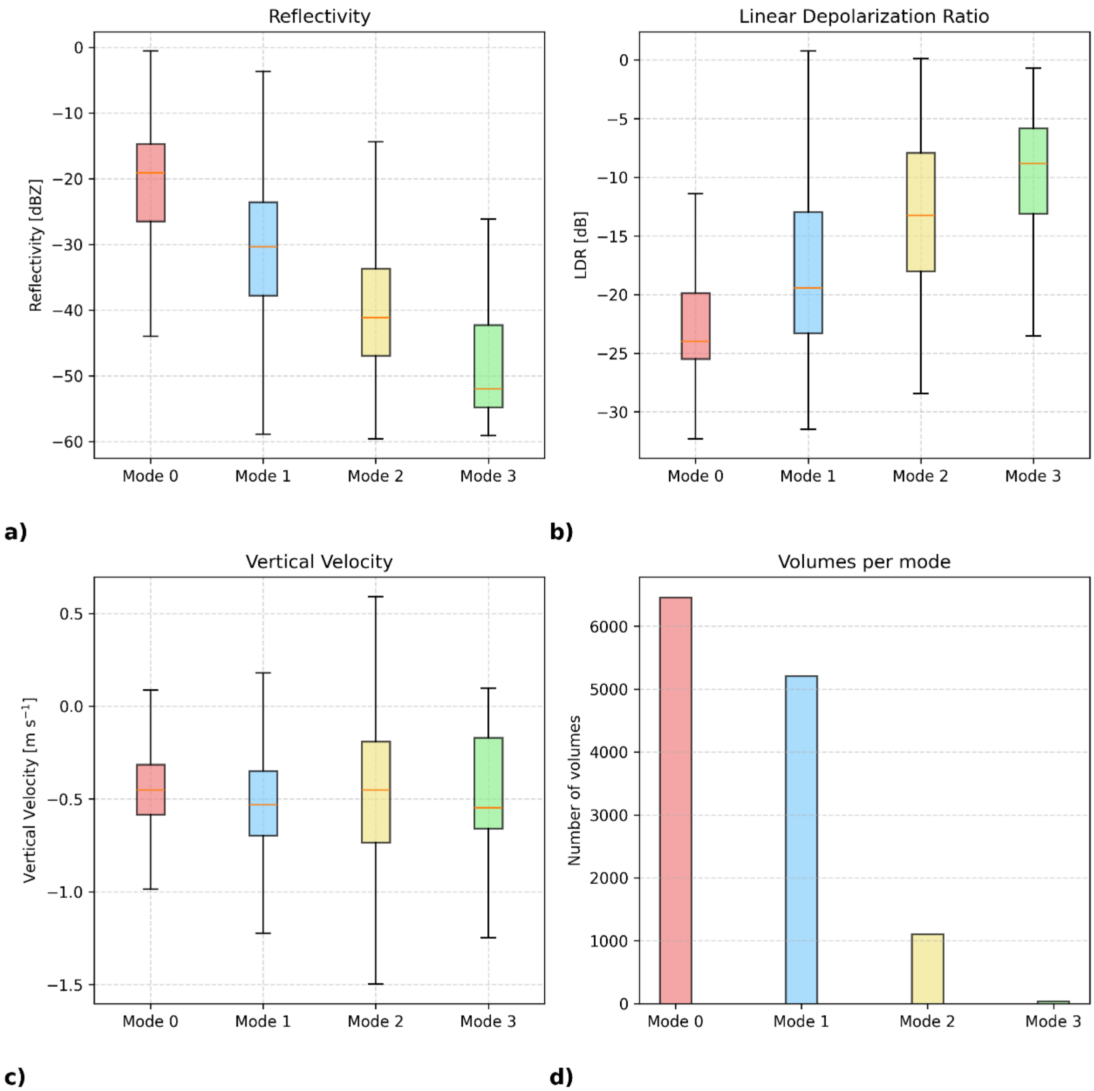

Figure E6. Same as Fig. E2 for the period 27 March 2024 6:00 –15:43 UTC.

575

https://doi.org/10.5194/essd-2026-549
Preprint. Discussion started: 10 September 2026

Case 28-31 March 2024

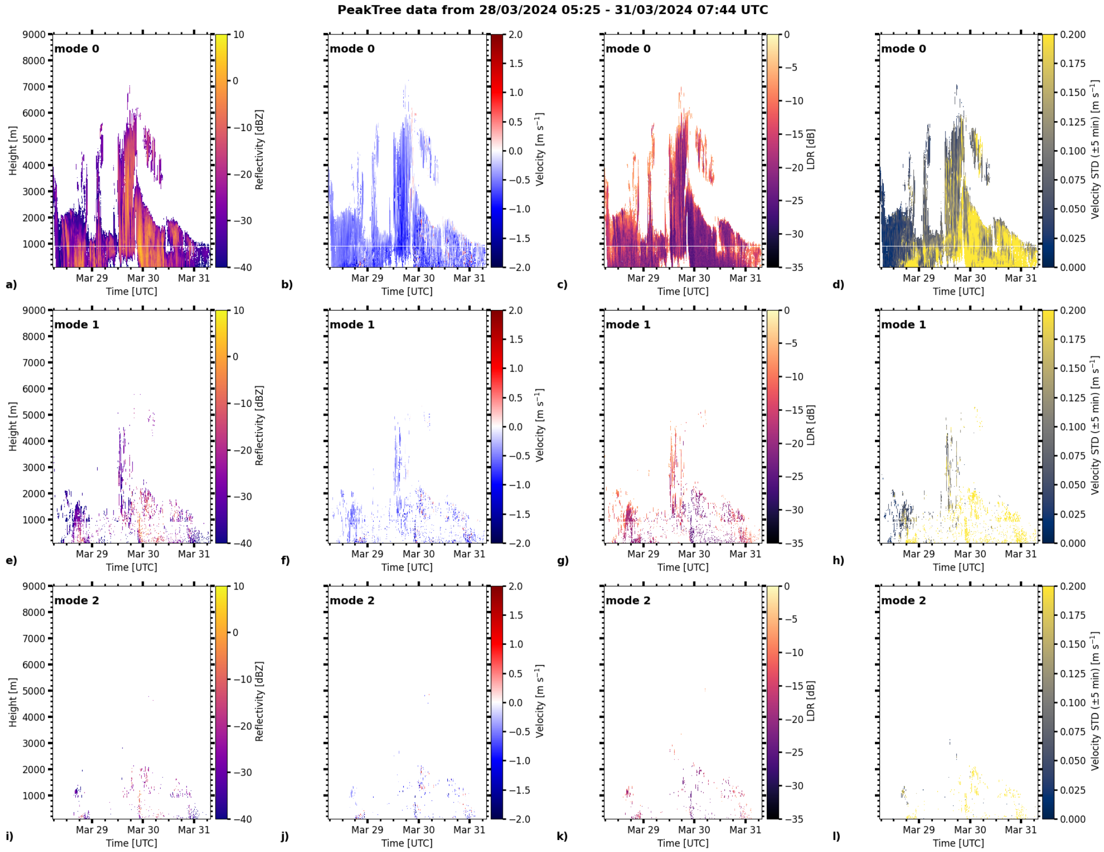

Figure E7. Same as Fig. E1 for the period 28 March 2024 5:25 – 31 March 2024 07:44 UTC.

https://doi.org/10.5194/essd-2026-549
Preprint. Discussion started: 10 September 2026

Open Access Earth System Science Data Discussions

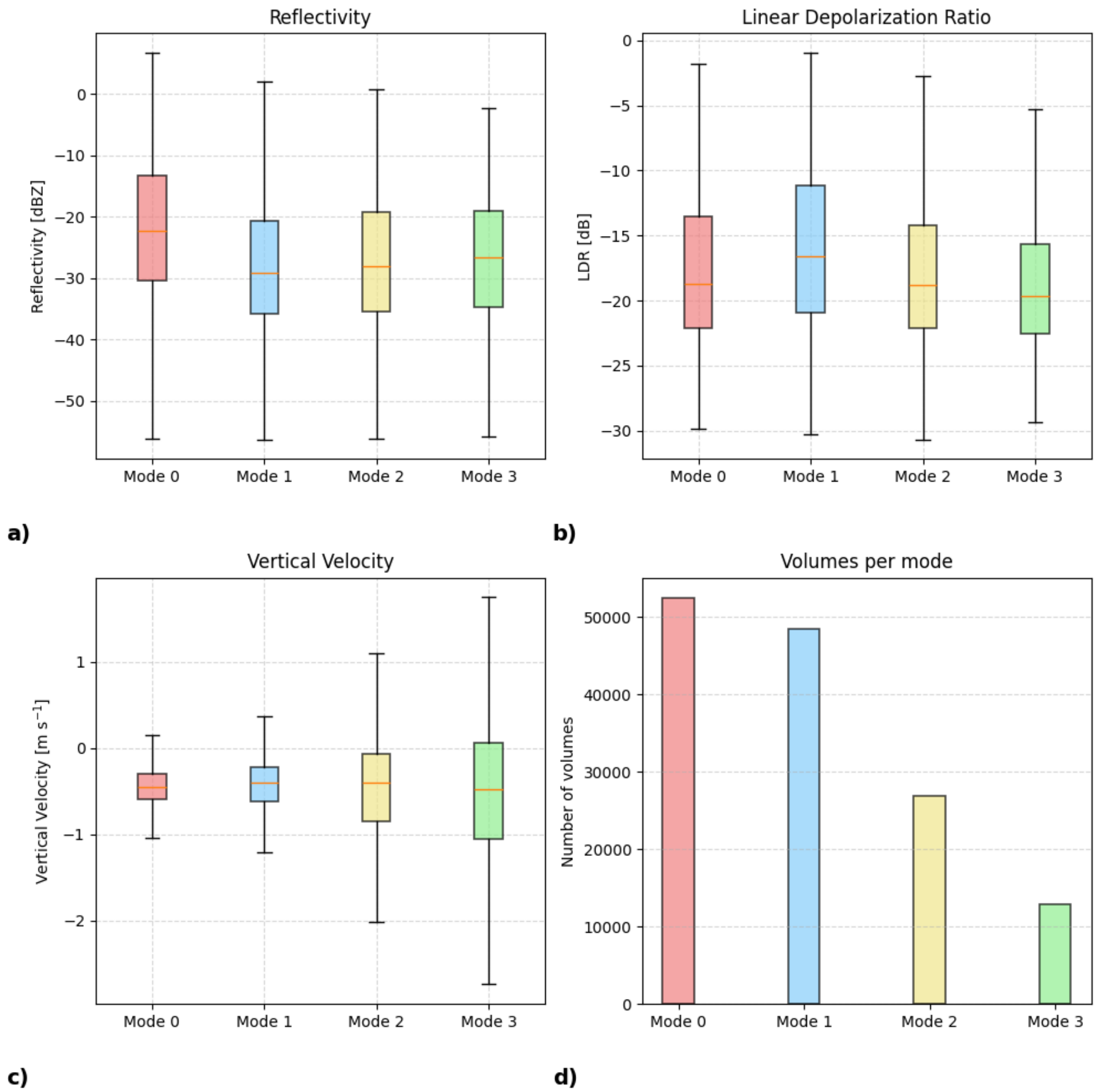

580 **Figure E8. Same as Fig. E2 for the period 28 March 2024 5:25 – 31 March 2024 07:44 UTC.**

https://doi.org/10.5194/essd-2026-549
Preprint. Discussion started: 10 September 2026

Case 1-5 April 2024

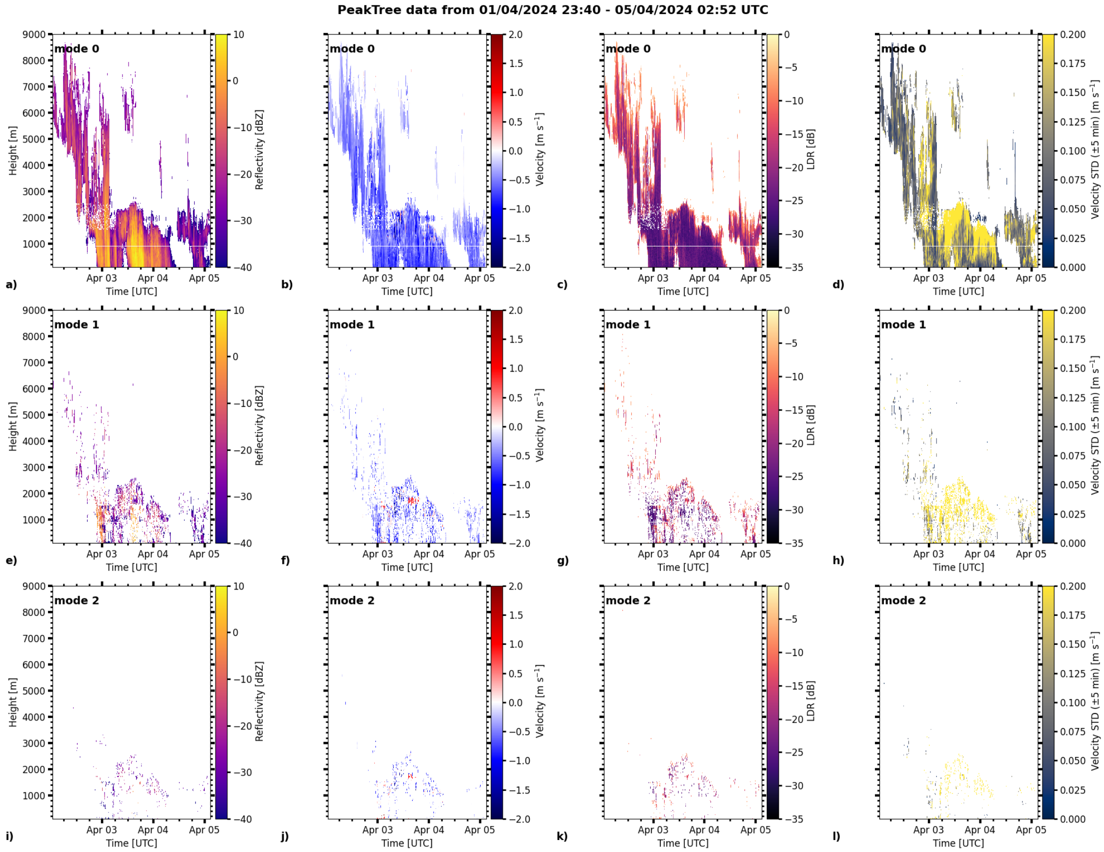

Figure E9. Same as Fig. E1 for the period 1 April 2024 23:40 – 5 April 2024 2:52 UTC.

https://doi.org/10.5194/essd-2026-549
Preprint. Discussion started: 10 September 2026

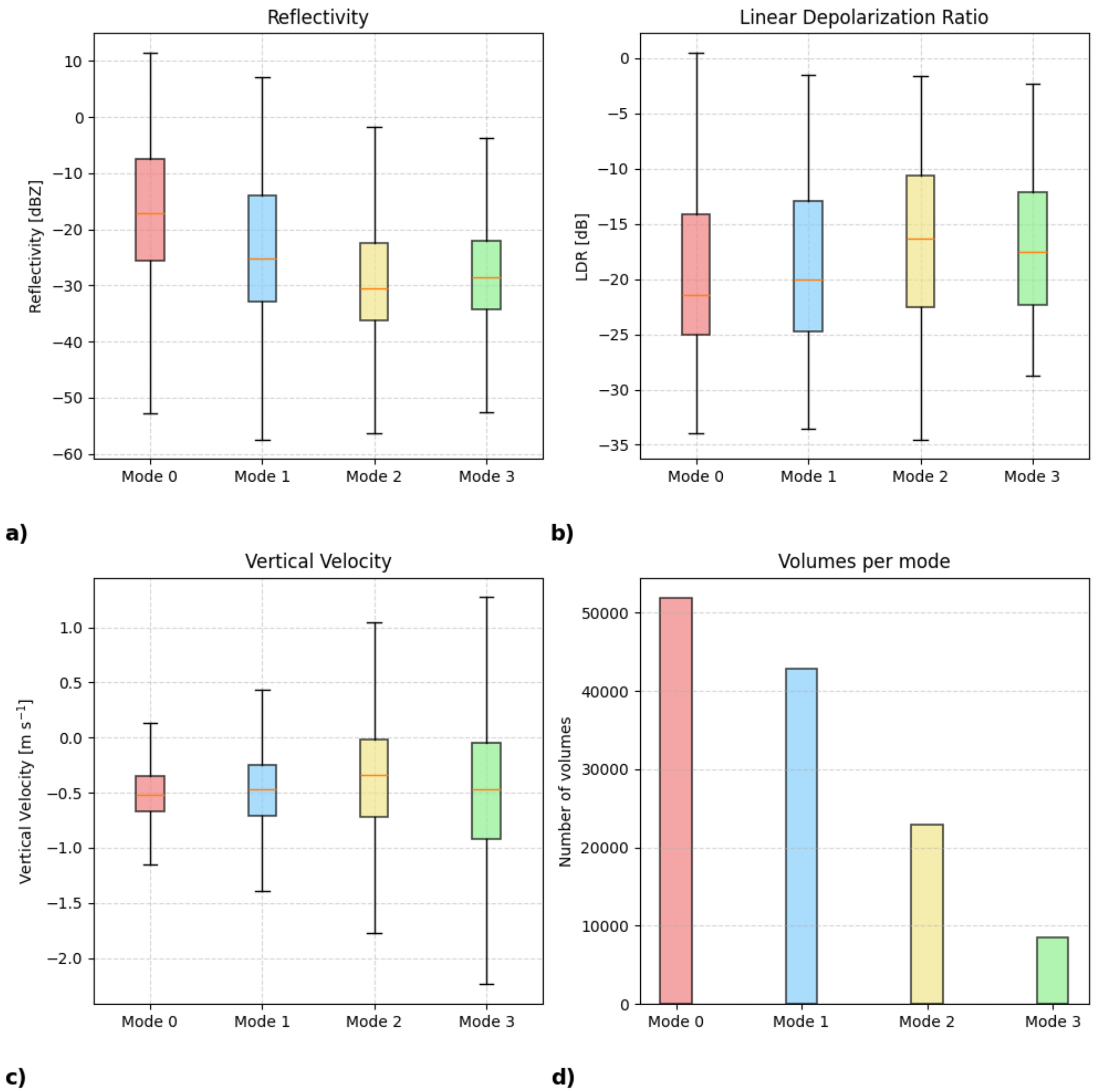

585

Figure E10. Same as Fig. E2 for the period 1 April 2024 23:40 – 5 April 2024 2:52 UTC.

https://doi.org/10.5194/essd-2026-549
Preprint. Discussion started: 10 September 2026

Case 8 April 2024

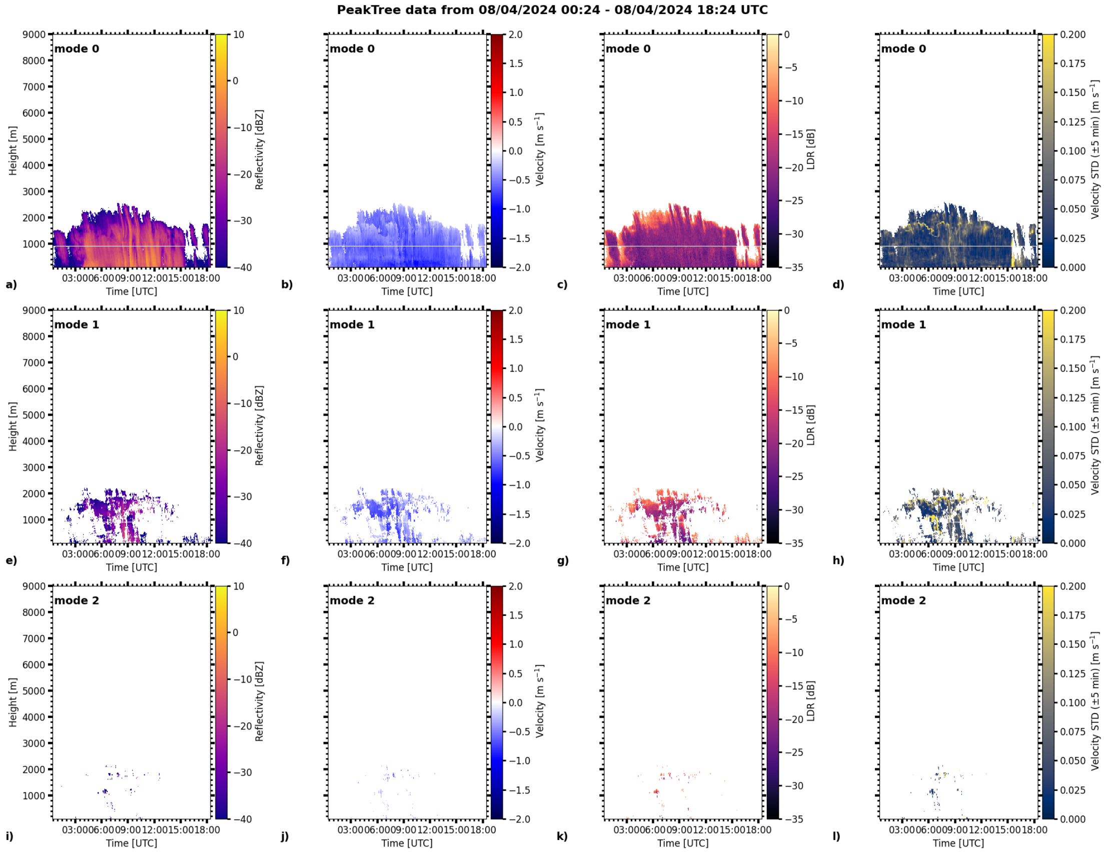

Figure E11. Same as Fig. E1 for the period 8 April 2024 0:24 – 18:24 UTC.

https://doi.org/10.5194/essd-2026-549
Preprint. Discussion started: 10 September 2026

Open Access Earth System Science Data Discussions

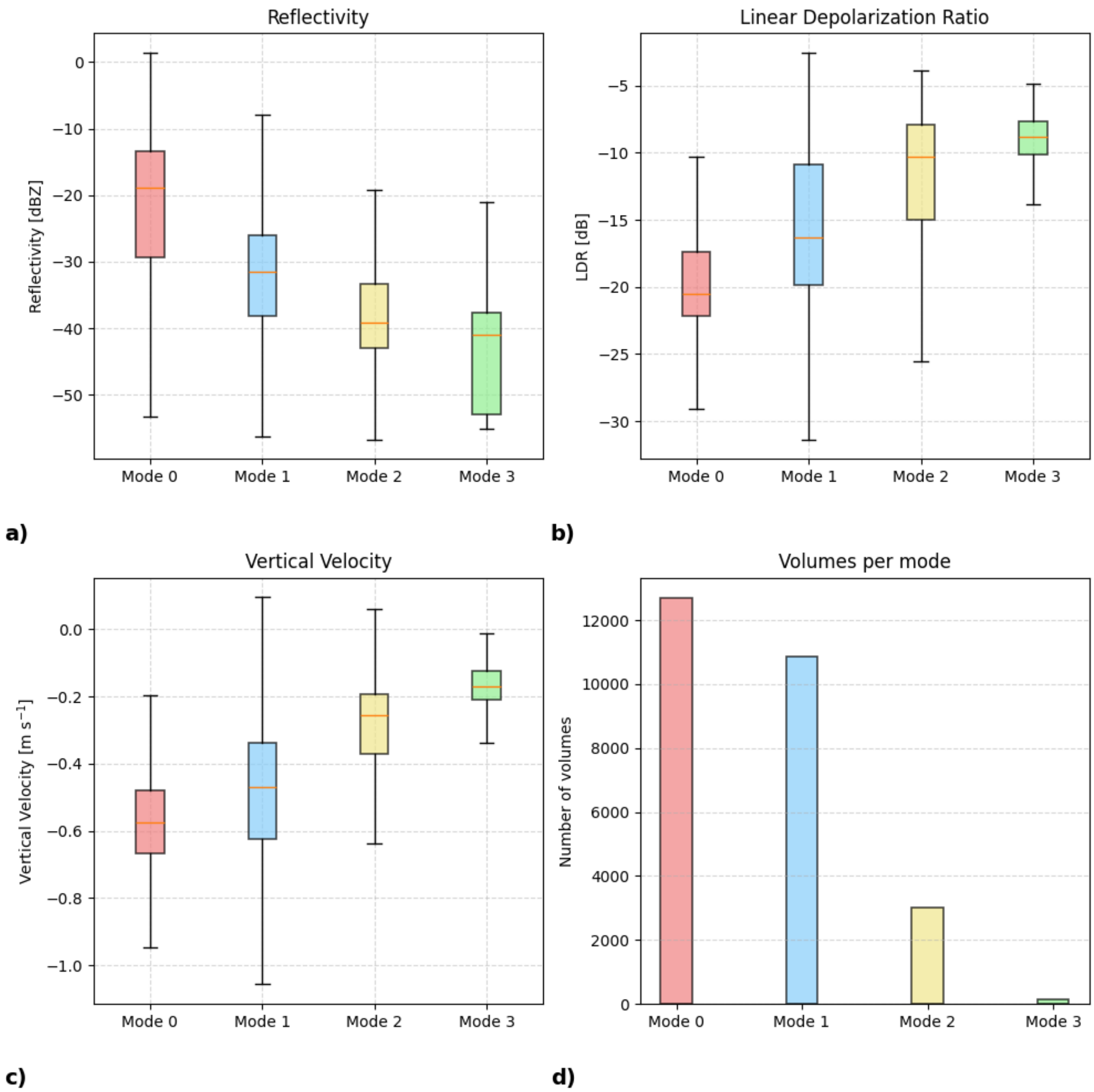

590 **Figure E12. Same as Fig. E2 for the period 8 April 2024 0:24 – 18:24 UTC.**

https://doi.org/10.5194/essd-2026-549
Preprint. Discussion started: 10 September 2026

Case 11-13 April 2024

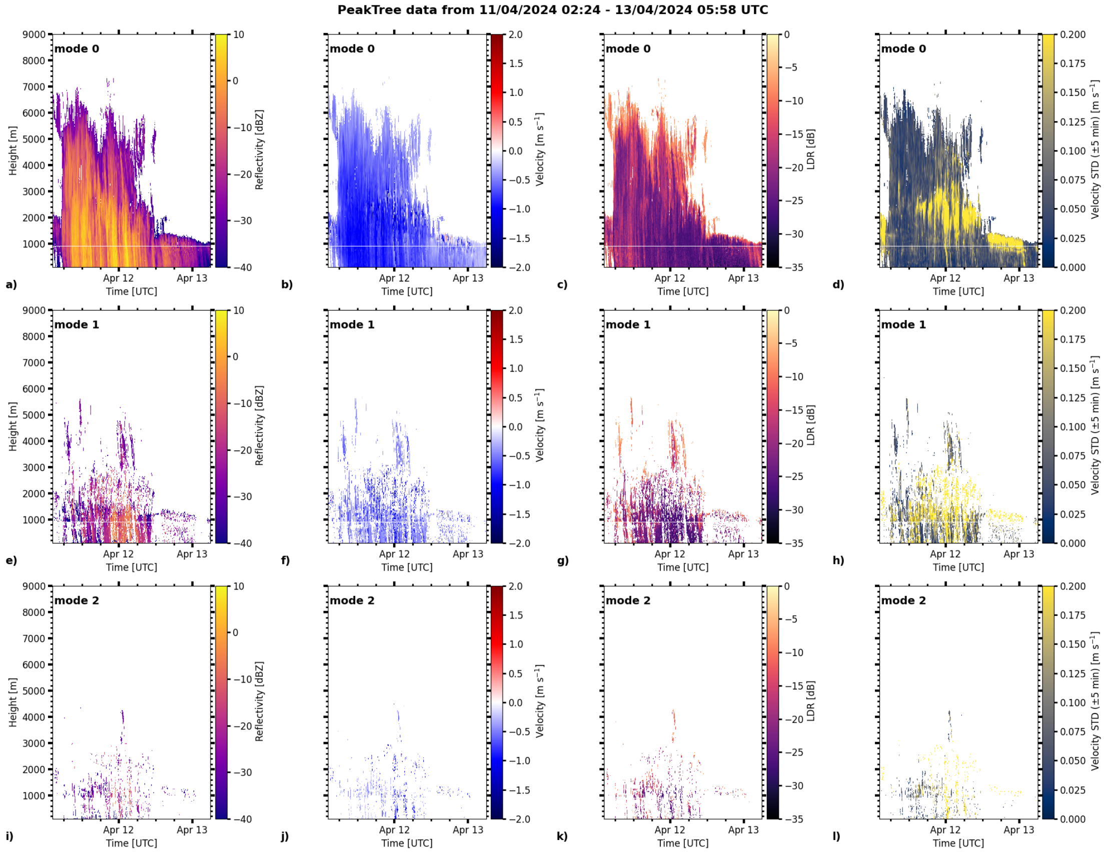

595 **Figure E13. Same as Fig. E1 for the period 11 April 2024 2:24 – 13 April 2024 5:58 UTC.**

https://doi.org/10.5194/essd-2026-549
Preprint. Discussion started: 10 September 2026

Open Access Earth System Science Data Discussions

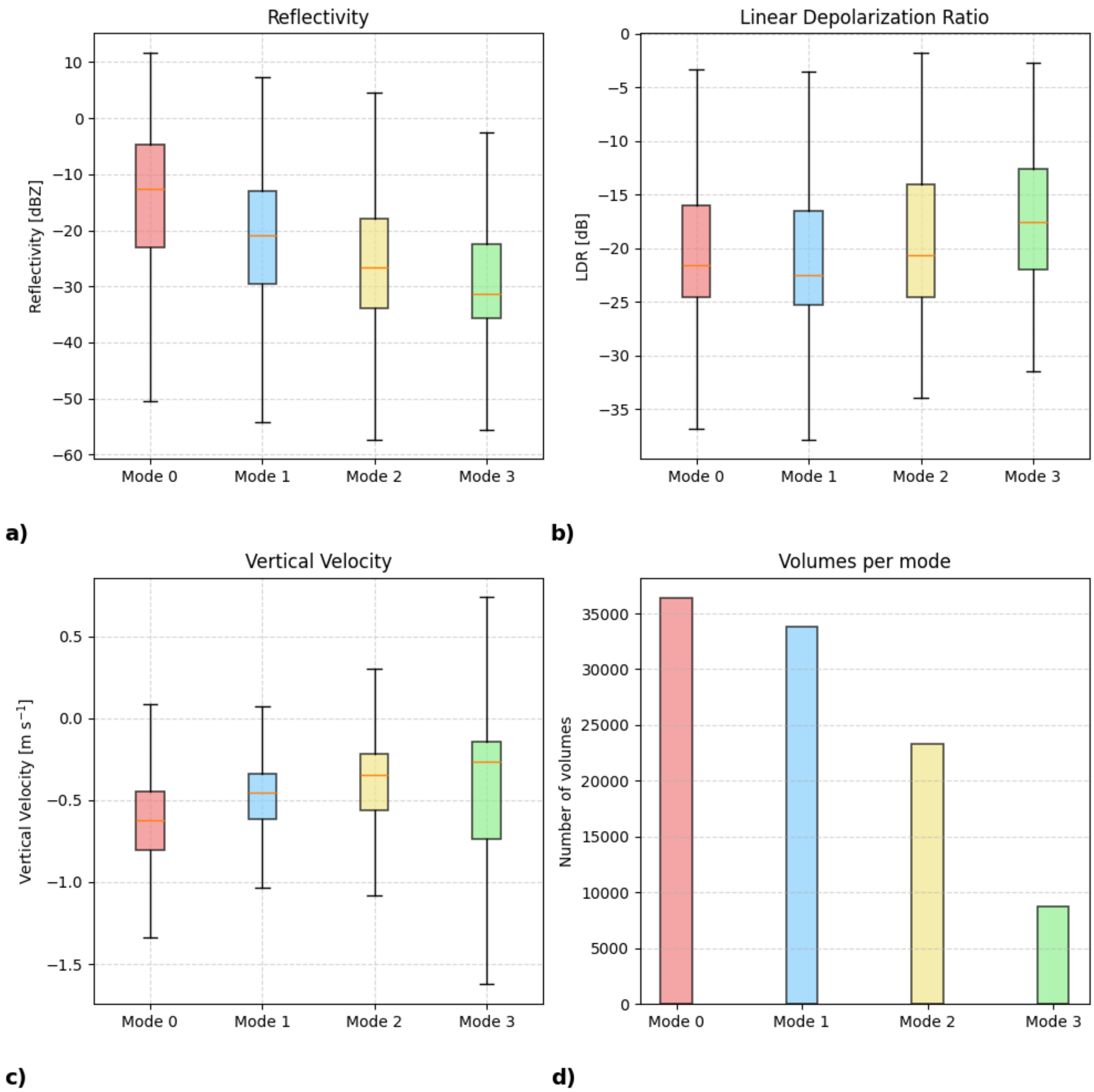

Figure E14. Same as Fig. E2 for the period 11 April 2024 2:24 – 13 April 2024 5:58 UTC.

Appendix F. Spectograms per case

The following figures present representative Doppler spectrograms selected for each case. The left panels show spectral reflectivity and the right panels spectral LDR, while dashed lines indicate ERA5 temperature contours and symbols identify the peakTree-resolved and the hydrometeor classes. Each spectrogram represents a single radar profile and should be interpreted together with the corresponding time–height figures.

https://doi.org/10.5194/essd-2026-549
Preprint. Discussion started: 10 September 2026

Case 23-25 March 2024

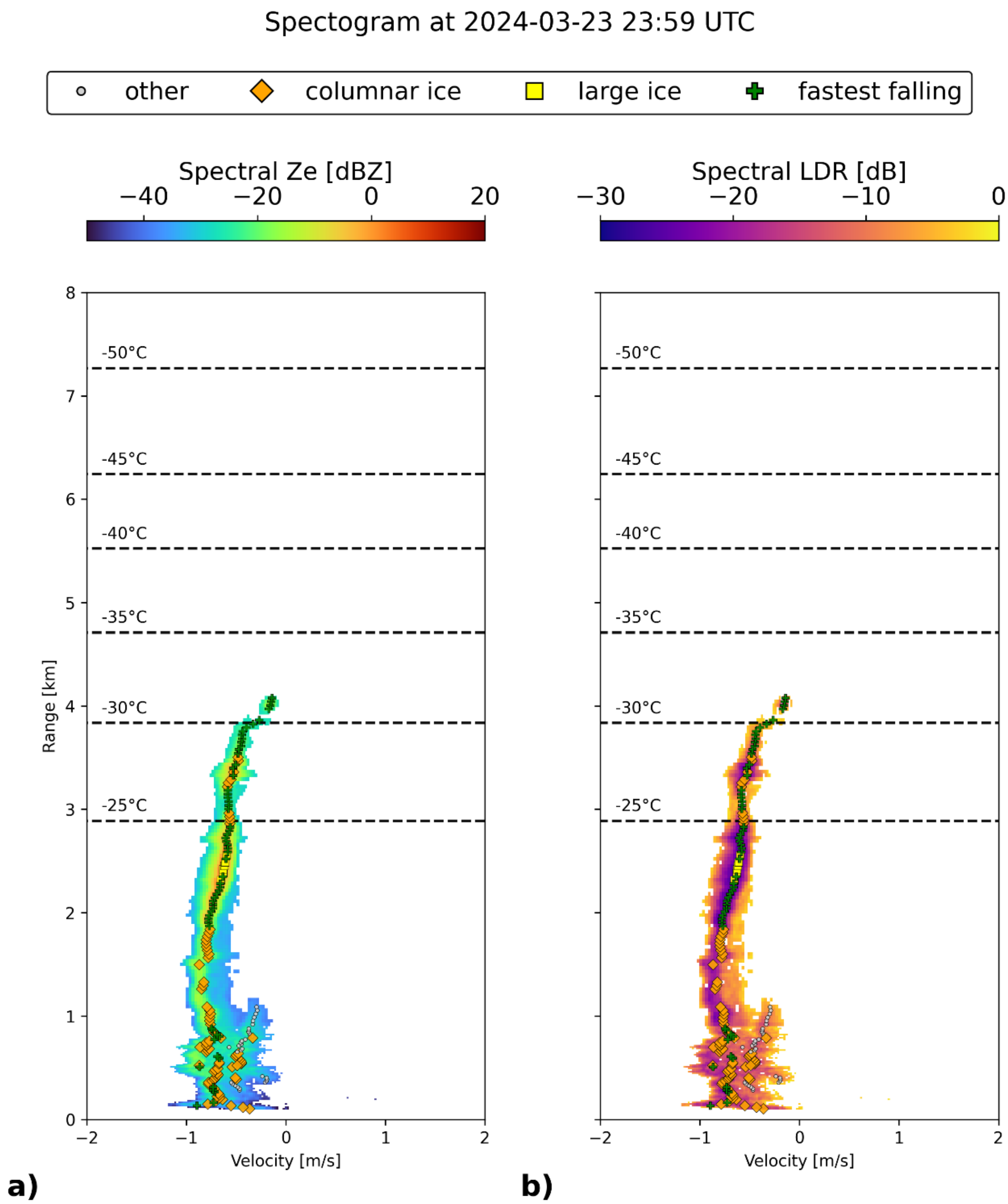

605 **Figure F1. a) Example of a Doppler spectrogram on 23 March 2024, 23:59 UTC, on which secondary modes identified by the peakTree decision tree are labelled. Colours indicate spectral radar reflectivity (Ze), b) Corresponding linear depolarisation ratio (LDR) spectrogram, together with the temperature contours (°C) obtained from ERA5. The white area surrounding the spectrograms denotes regions where the cross-polar signal is below the noise level. Symbols indicate the corresponding modes obtained from the peakTree classification, marking hydrometeor classes including columnar ice, large ice, and the fastest-falling**
610 **particles.**

https://doi.org/10.5194/essd-2026-549
Preprint. Discussion started: 10 September 2026

Case 25-26 March 2024

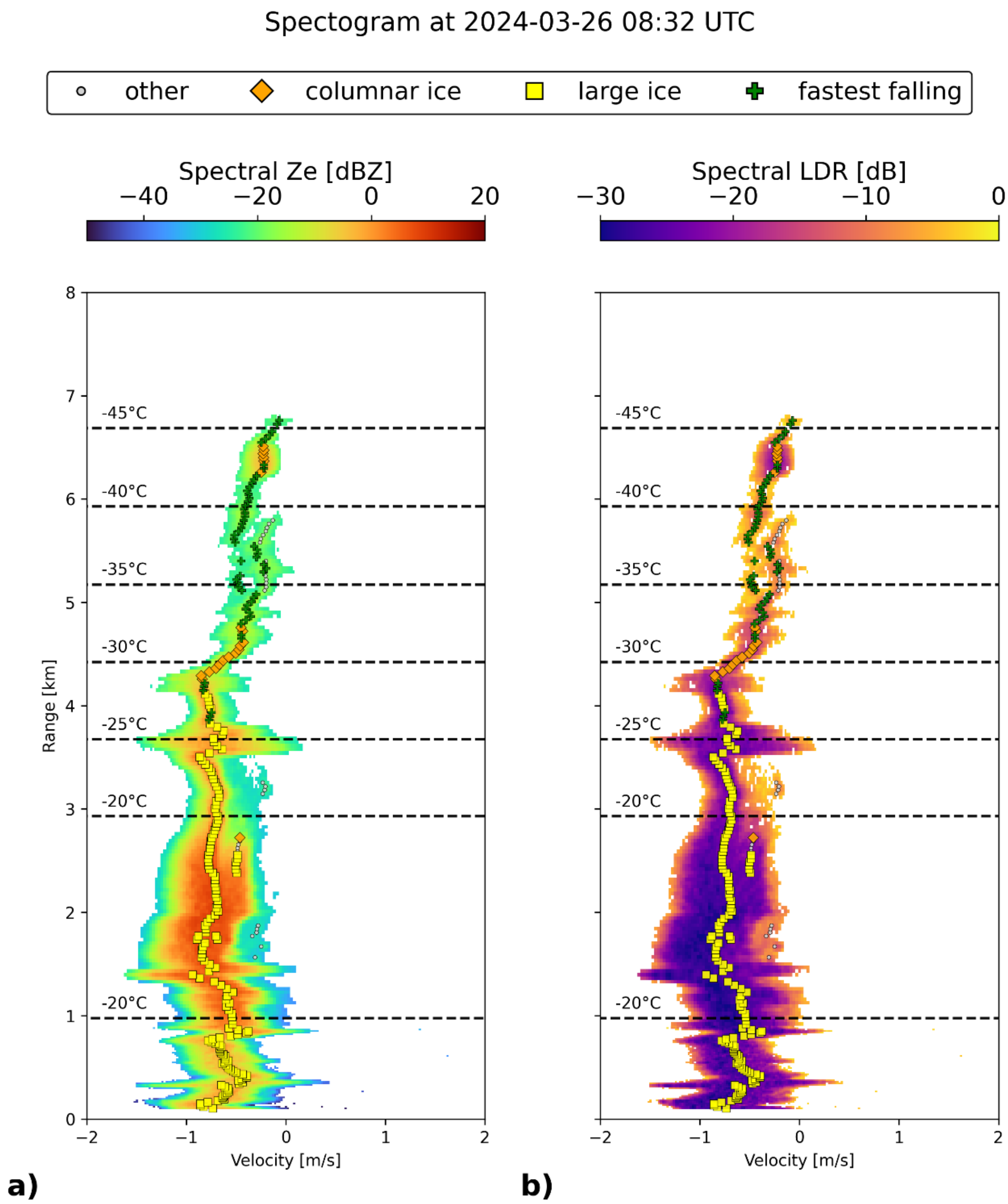

Figure F2. Same as Fig. F1 for 26 March 2024, 8:32 UTC.

https://doi.org/10.5194/essd-2026-549
Preprint. Discussion started: 10 September 2026

Case 27 March 2024

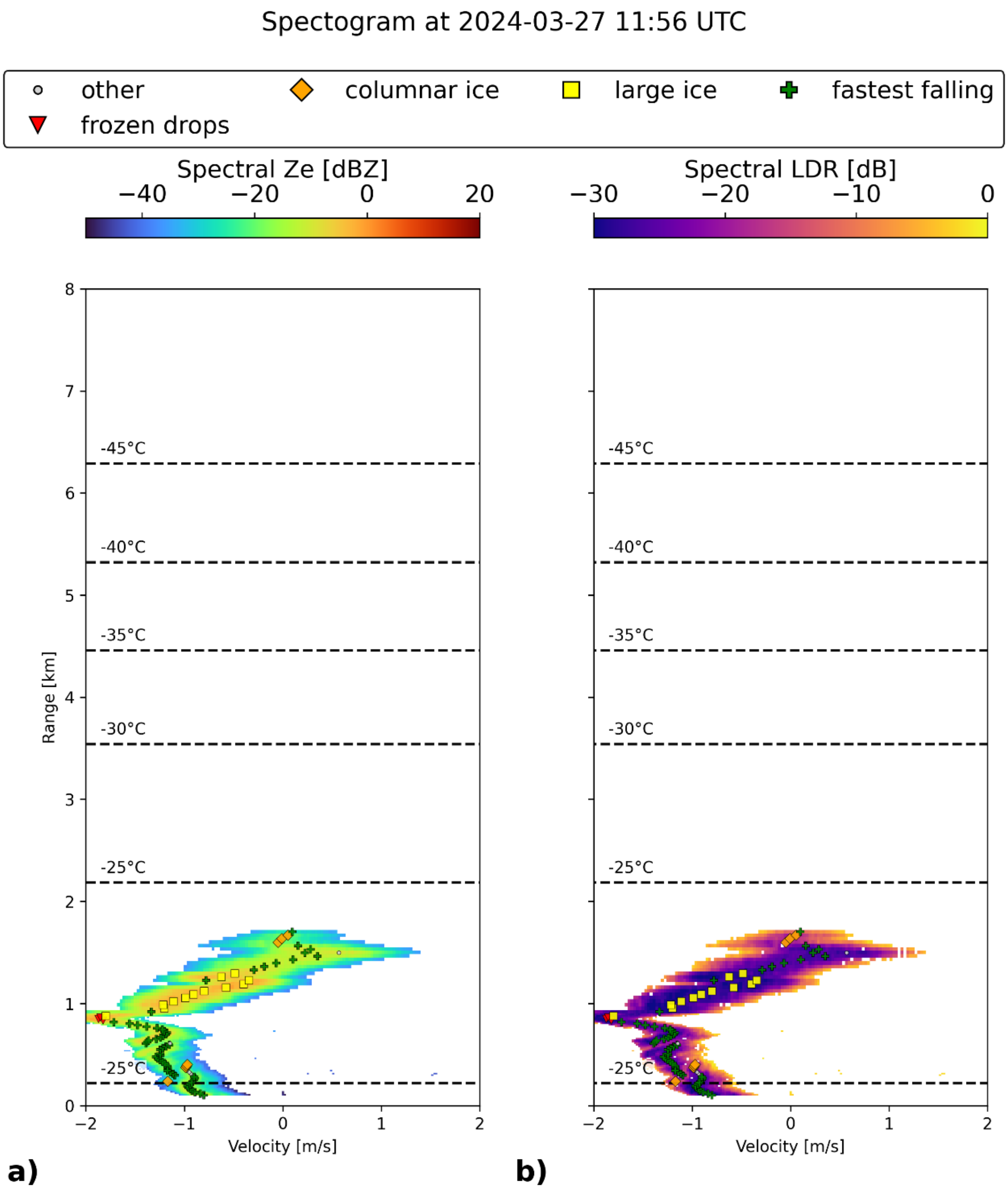

615

Figure F3. Same as Fig. F1 for 26 March 2024, 11:56 UTC.

https://doi.org/10.5194/essd-2026-549
Preprint. Discussion started: 10 September 2026

Case 28-31 March 2024

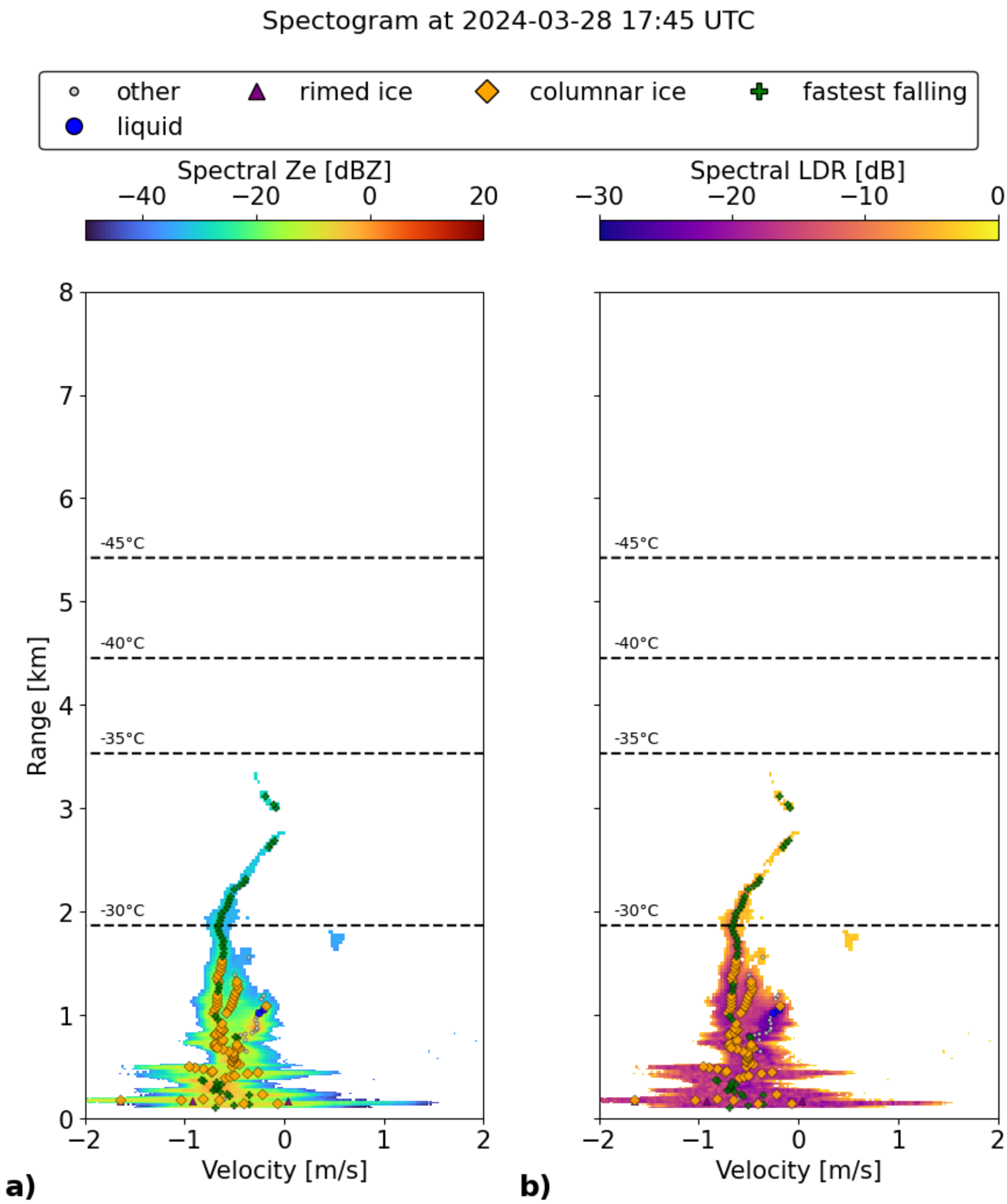

Figure F4. Same as Fig. F1 for 28 March 2024, 17:45 UTC.

620

https://doi.org/10.5194/essd-2026-549
Preprint. Discussion started: 10 September 2026

Open Access Earth System Science Data Discussions

Case 1-5 April 2024

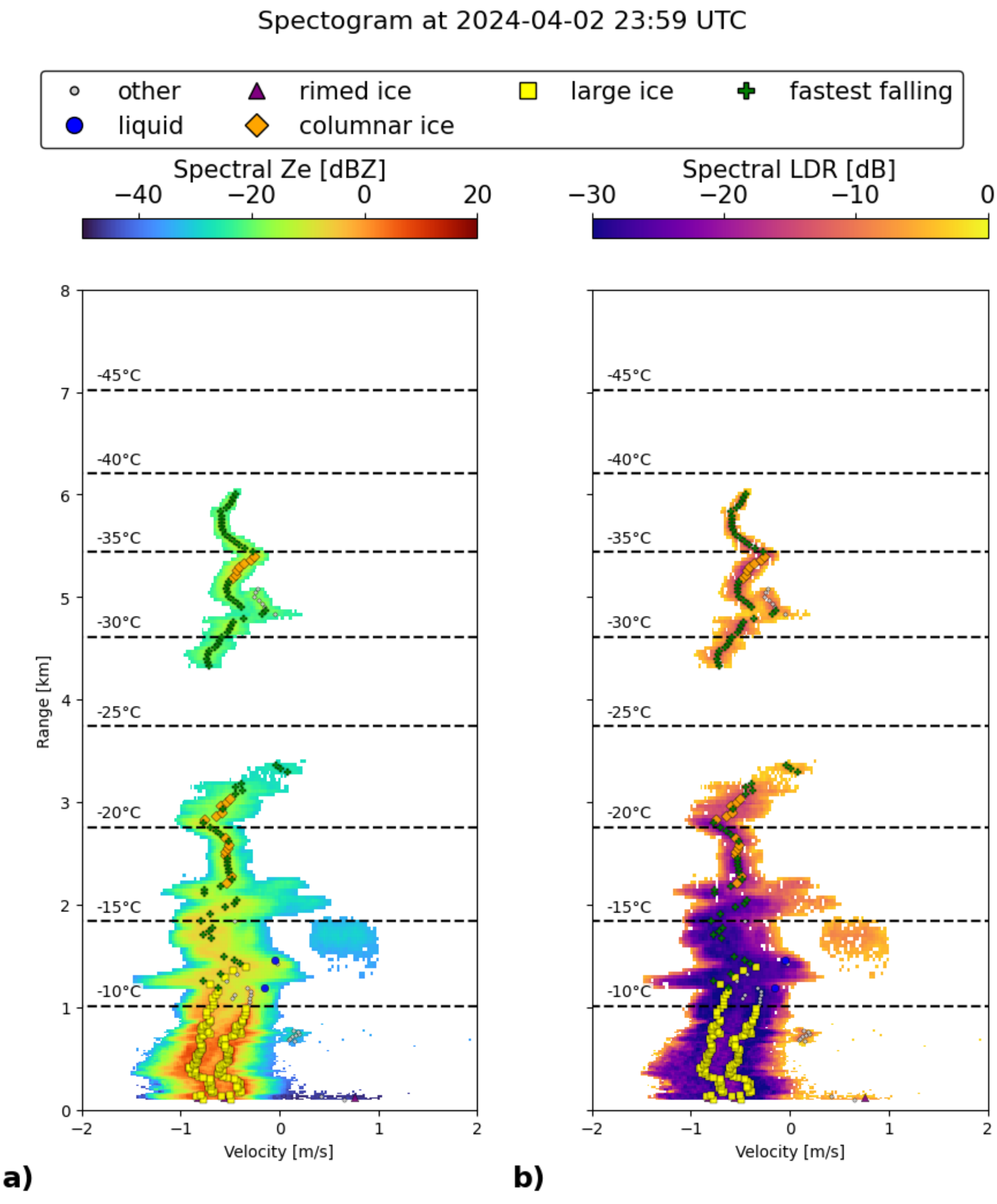

Figure F5. Same as Fig. F1 for 2 April 2024, 23:59 UTC.

https://doi.org/10.5194/essd-2026-549
Preprint. Discussion started: 10 September 2026

625 **Case 8 April 2024**

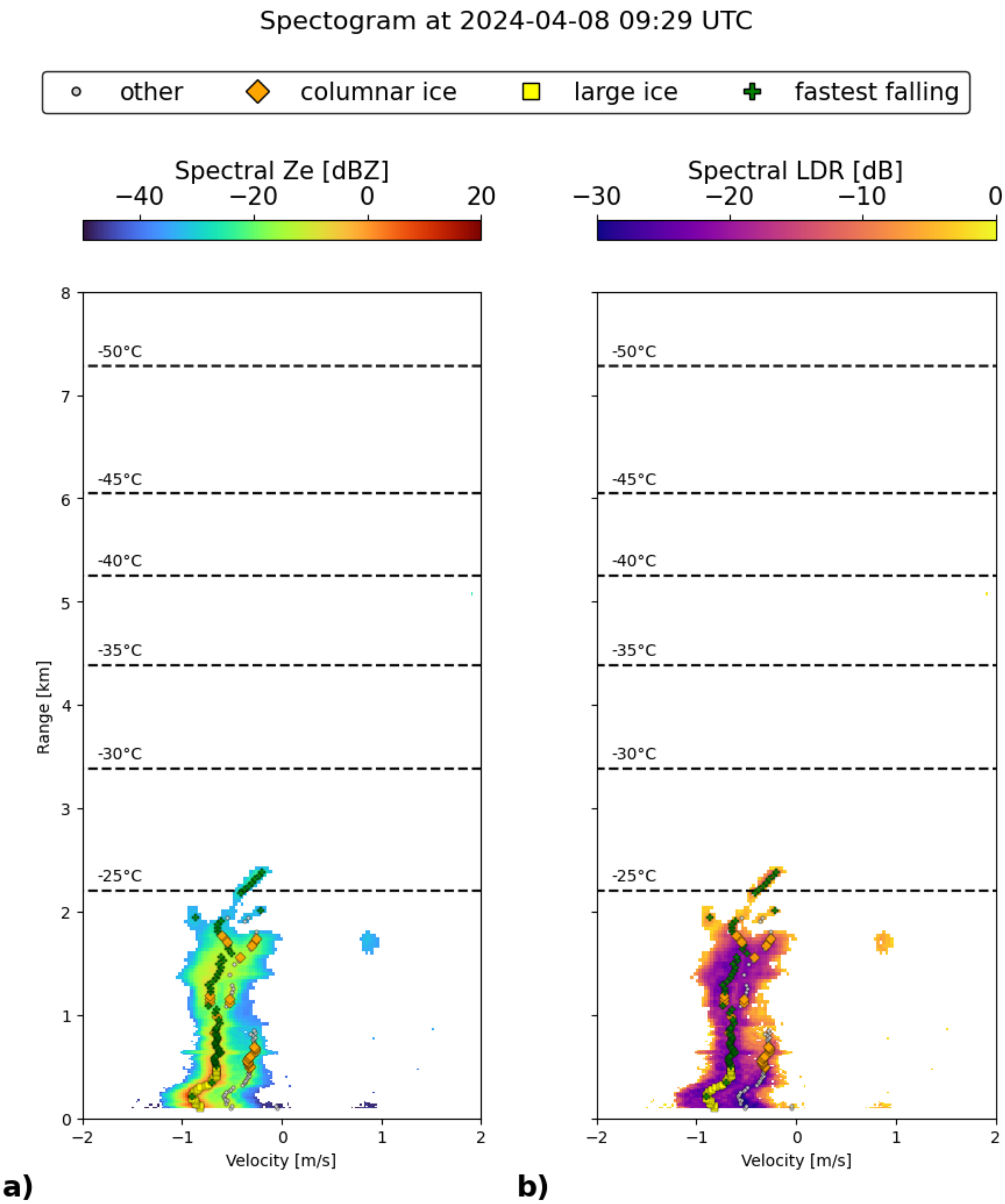

Figure F6. Same as Fig. F1 for 8 April 2024, 9:29 UTC.

https://doi.org/10.5194/essd-2026-549
Preprint. Discussion started: 10 September 2026

Case 11-13 April 2024

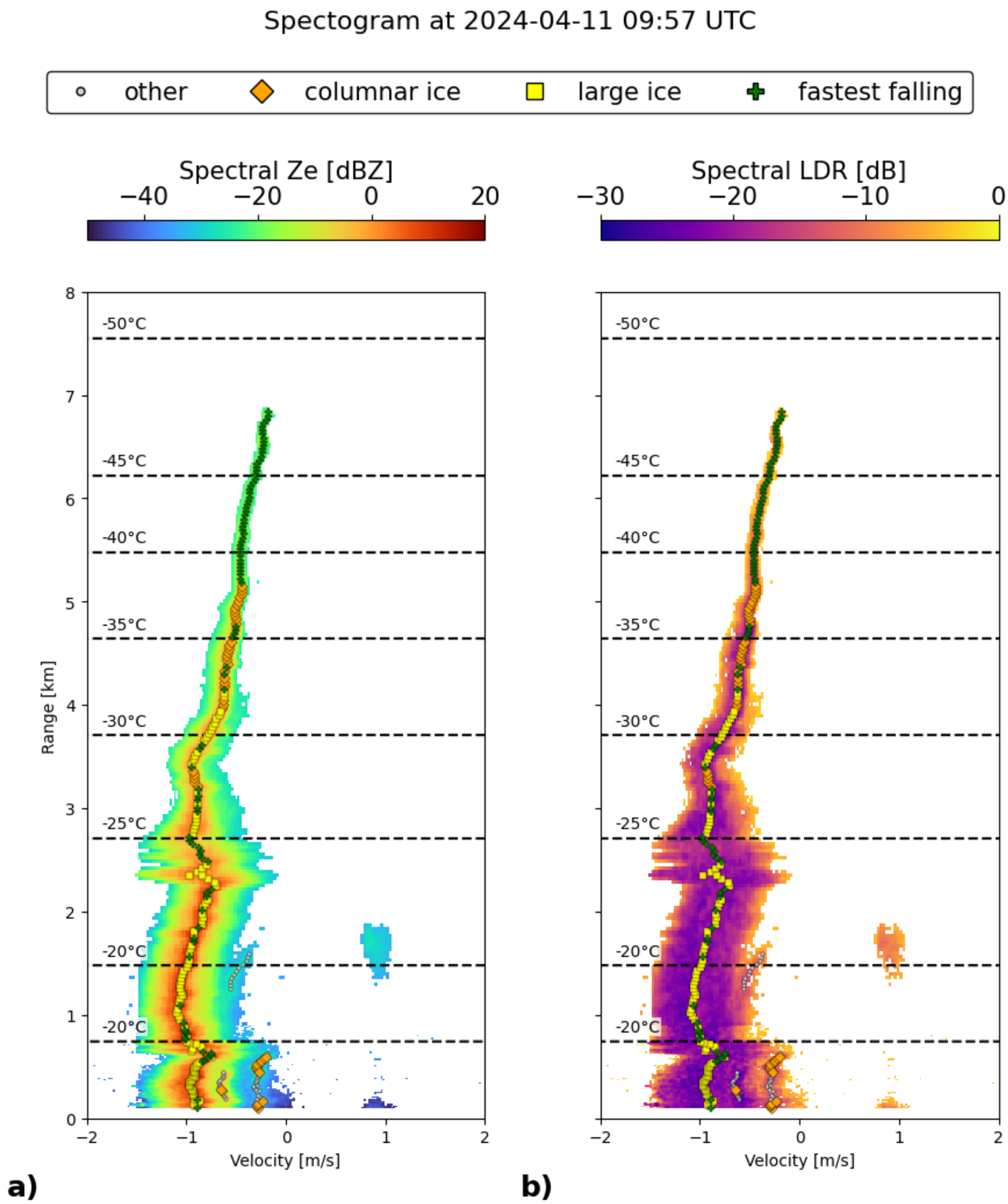

630

Figure F7. Same as Fig. F1 for 11 April 2024, 9:57 UTC.

https://doi.org/10.5194/essd-2026-549
Preprint. Discussion started: 10 September 2026

Open Access Earth System Science Data Discussions

Data Availability

Overview of the dataset

The measurements presented in this study were acquired using the Doppler non-scanning cloud radar LTE RPG-FMCW-94-DP, whose instrument metadata are publicly available through the ACTRIS Cloudnet Portal (Berne and Foskinis, 2026a). The publicly available dataset includes the raw radar files (.LV0), Level 1 radar products, and peakTree output files (.nc4). It consists of peak-resolved Doppler spectral products derived from continuous W-band cloud radar measurements collected during the CLAVIER campaign at Villum Research Station. The dataset spans the full duration of the campaign and contains time–height profiles of Doppler spectra processed independently for each radar chirp. For every time–range gate, the peakTree algorithm was applied to the pre-processed Doppler spectra to identify and characterize multiple spectral modes within a single radar sampling volume. Each spectral mode represents a distinct hydrometeor population coexisting at the same height and time. In addition to the radar and peakTree products, a supplementary dataset containing integrated water vapor and liquid water path retrievals is provided in standalone NetCDF files. The dataset includes the native radiometer retrievals together with six alternative liquid water path retrievals produced using the pyLWP neural-network framework, representing different combinations of auxiliary predictors (ERA5-derived and/or surface meteorological variables). The retrievals are based on brightness temperatures radiometrically calibrated using forward simulations constrained by radiosonde observations (Dorff et al., 2026), following the methodology of Billault-Roux and Berne (2021). The complete dataset is publicly available through the ACTRIS Cloudnet Portal at https://doi.org/10.60656/7aa872e5b5f84583 (Berne and Foskinis, 2026b).

Data content

For each detected spectral mode, the dataset provides a comprehensive set of mode-resolved radar variables, including:

- radar equivalent reflectivity factor (Ze_m)
- mean Doppler velocity (MDV_m)
- spectral width
- peak prominence
- skewness and kurtosis of the spectral mode
- signal-to-noise ratio (SNR)
- linear depolarization ratio (LDR_m) and maximum LDR ($LDRmax_m$)
- peak boundaries in Doppler velocity space
- Integrated water vapor (IWV) and multiple liquid water path (LWP) retrievals, including:
- Integrated-water-vapor
- Liquid-water-path (native radiometer retrieval)
- Liquid-water-path-pyLWP-ERA_noGeo_Surf

https://doi.org/10.5194/essd-2026-549
Preprint. Discussion started: 10 September 2026

Open Access Earth System Science Data Discussions

- Liquid-water-path-pyLWP-ERA_Geo_Surf
- Liquid-water-path-pyLWP-ERA_Geo_noSurf
- Liquid-water-path-pyLWP-noERA_noGeo_Surf
- Liquid-water-path-pyLWP-noERA_Geo_Surf
- Liquid-water-path-pyLWP-noERA_Geo_noSurf

In addition to the peak-resolved quantities, the dataset includes the cleaned and smoothed co- and cross-polarized Doppler spectra used as input to the peak detection algorithm, together with associated noise levels, detection thresholds, and quality masks. These auxiliary variables allow full traceability of the peak detection process and facilitate reproducibility and sensitivity analyses.

Data content

The dataset is provided in NetCDF4 format and follows a hierarchical structure organized by time, range, chirp index, and spectral mode. Time is given in UTC, and heights are referenced to mean sea level. All variables include standard metadata describing units, dimensions, and processing steps. The supplementary pyLWP dataset is distributed as standalone daily NetCDF4 files with a common time coordinate, allowing straightforward integration with the radar observations while remaining independent of the original W-band radar files.

Author contributions

RF wrote the paper, developed the data processing, and analyzed and visualized the data. AN and AB designed the experiment. AB supervised the analysis and the writing of the paper. A.-C. B.-R. contributed to the development of the data processing, radar calibration, and analysis. All co-authors contributed to the review of the manuscript.

Competing interests

The authors declare that they have no conflict of interest.

Disclaimer

Copernicus Publications remains neutral with regard to jurisdictional claims made in the text, published maps, institutional affiliations, or any other geographical representation in this paper. While Copernicus Publications makes every effort to include appropriate place names, the final responsibility lies with the authors. Views expressed in the text are those of the authors and do not necessarily reflect the views of the publisher.

https://doi.org/10.5194/essd-2026-549
Preprint. Discussion started: 10 September 2026

Acknowledgements

The authors acknowledge the logistical support provided at Villum Research Station and Station Nord in Northeast Greenland. We also thank Jørgen Skafte and Bjarne Jensen for their support provided at VRS. The CLAVIER campaign was conducted within the framework of the CleanCloud project (Clouds and climate transitioning to post-fossil aerosol regime), funded by the Horizon Europe Programme of the European Union (Grant Agreement no. 101137639). We also acknowledge the ACTRIS Cloudnet Portal for hosting the datasets. The authors used ChatGPT (OpenAI) to assist with language editing and to support code development during data processing and visualization. All analyses, scientific interpretations, and the final manuscript content were reviewed, verified, and approved by the authors.

Financial support

Funded by the Horizon Europe Programme of the European Union (Grant Agreement no. 101137639)

References

Achtert, P., Seelig, T., Wallentin, G., Ickes, L., Shupe, M. D., Hoose, C., & Tesche, M. (2025). Occurrence of seeding multi-layer clouds in the Arctic from ground-based observations. EGUsphere, 1–29. https://doi.org/10.5194/egusphere-2025-3529

Berne, A. and Foskinis, R.: Doppler non-scanning cloud radar LTE RPG-FMCW-94-DP (WProf). (instrument) École Polytechnique Fédérale de Lausanne (EPFL), https://hdl.handle.net/21.12132/3.cec71b56a8444a48, 2026a.

Berne, A. and Foskinis, R.: Custom collection of radar data from Villum between 22 Mar and 13 Apr 2024, https://doi.org/10.60656/7AA872E5B5F84583, 2026b.

Billault-Roux, A.-C., & Berne, A. (2021). Integrated water vapor and liquid water path retrieval using a single-channel radiometer. Atmospheric Measurement Techniques, 14(4), 2749–2769. https://doi.org/10.5194/amt-14-2749-2021

Billault-Roux, A.-C., Georgakaki, P., Gehring, J., Jaffeux, L., Schwarzenboeck, A., Coutris, P., Nenes, A., & Berne, A. (2023). Distinct secondary ice production processes observed in radar Doppler spectra: insights from a case study. Atmospheric Chemistry and Physics, 23(17), 10207–10234. https://doi.org/10.5194/acp-23-10207-2023

Bühl, J., Radenz, M., Schimmel, W., Vogl, T., Röttenbacher, J., & Lochmann, M. (2021). pyLARDA v3.2. https://doi.org/10.5281/ZENODO.4721311

Bühl, J., Seifert, P., Myagkov, A., & Ansmann, A. (2016). Measuring ice-and liquid-water properties in mixed-phase cloud layers at the Leipzig Cloudnet station. Atmospheric Chemistry and Physics, 16(16), 10609–10620. https://doi.org/10.5194/acp-16-10609-2016

https://doi.org/10.5194/essd-2026-549
Preprint. Discussion started: 10 September 2026

Chellini, G., Gierens, R., Ebell, K., Kiszler, T., Krobot, P., Myagkov, A., Schemann, V., & Kneifel, S. (2023). Low-level mixed-phase clouds at the high Arctic site of Ny-Alesund: A comprehensive long-term dataset of remote sensing observations. Earth System Science Data, 15(12), 5427–5448. https://doi.org/10.5194/essd-15-5427-2023

Dorff, H., Müller, J., Siebert, H., Schäfer, M., Ehrlich, A., & Wendisch, M. (2026). Daily radiosonde profile measurement data complementing balloon-borne measurements at Villum Research Station for characterising the Arctic atmospheric boundary layer [dataset].

Gryning, S. E., Batchvarova, E., Floors, R., Münkel, C., Sørensen, L. L., & Skov, H. (2023). Observed aerosol-layer depth at Station Nord in the high Arctic. International Journal of Climatology, 43(7), 3247–3263. https://doi.org/10.1002/JOC.8027

Heidam, N., Christensen, J., Wahlin, P., & Skov, H. (2004). Arctic atmospheric contaminants in NE Greenland: levels, variations, origins, transport, transformations and trends 1990–2001. Science of The Total Environment, 331(1–3), 5–28. https://doi.org/10.1016/j.scitotenv.2004.03.033

Hersbach, H., Bell, B., Berrisford, P., Biavati, G., Horányi, A., Sabater Muñoz, J., Nicolas, J., Peubey, C., Radu, R., Rozum, I., Schepers, D., Simmons, A., Soci, C., Dee, D., & Thépaut, J.-N. (2018). ERA5 hourly data on pressure levels from 1979 to present. Copernicus Climate Change Service (C3S) Climate Data Store (CDS). (Accessed on 01-Jan-2021). https://doi.org/10.24381/cds.bd0915c6

Hildebrand, P. H., & Sekhon, R. S. (1974). Objective Determination of the Noise Level in Doppler Spectra. Journal of Applied Meteorology, 13(7), 808–811. https://doi.org/10.1175/1520-0450(1974)013<0808:ODOTNL>2.0.CO;2

Illingworth, A. J., Hogan, R. J., O'Connor, E. J., Bouniol, D., Brooks, M. E., Delanoé, J., Donovan, D. P., Eastment, J. D., Gaussiat, N., Goddard, J. W. F., Haeffelin, M., Baltink, H. K., Krasnov, O. A., Pelon, J., Piriou, J.-M., Protat, A., Russchenberg, H. W. J., Seifert, A., Tompkins, A. M., … Wrench, C. L. (2007). Cloudnet: Continuous Evaluation of Cloud Profiles in Seven Operational Models Using Ground-Based Observations. Bulletin of the American Meteorological Society, 88(6), 883–898. https://doi.org/10.1175/BAMS-88-6-883

International Telecommunication Union. (2022). Recommendation ITU-R P.676-13: Attenuation by atmospheric gases and related effects. https://www.itu.int/dms_pubrec/itu-r/rec/p/R-REC-P.676-13-202208-I!!PDF-E.pdf

Kalesse, H., Szyrmer, W., Kneifel, S., Kollias, P., & Luke, E. (2016). Fingerprints of a riming event on cloud radar Doppler spectra: Observations and modeling. Atmospheric Chemistry and Physics, 16(5), 2997–3012. https://doi.org/10.5194/acp-16-2997-2016

Kalesse, H., Vogl, T., Paduraru, C., & Luke, E. (2019). Development and validation of a supervised machine learning radar Doppler spectra peak-finding algorithm. Atmospheric Measurement Techniques, 12(8), 4591–4617. https://doi.org/10.5194/AMT-12-4591-2019

Küchler, N., Kneifel, S., Löhnert, U., Kollias, P., Czekala, H., Rose, T., Küchler, N., Kneifel, S., Löhnert, U., Kollias, P., Czekala, H., & Rose, T. (2017). A W-Band Radar–Radiometer System for Accurate and Continuous Monitoring of Clouds and Precipitation. Journal of Atmospheric and Oceanic Technology, 34(11), 2375–2392. https://doi.org/10.1175/JTECH-D-17-0019.1

https://doi.org/10.5194/essd-2026-549
Preprint. Discussion started: 10 September 2026

Lange, R., Dall'Osto, M., Skov, H., Nøjgaard, J. K., Nielsen, I. E., Beddows, D. C. S., Simo, R., Harrison, R. M., & Massling, A. (2018). Characterization of distinct Arctic aerosol accumulation modes and their sources. Atmospheric Environment, 183, 1–10. https://doi.org/10.1016/j.atmosenv.2018.03.060

Lohmann, U., & Neubauer, D. (2018). The importance of mixed-phase and ice clouds for climate sensitivity in the global aerosol-climate model ECHAM6-HAM2. Atmospheric Chemistry and Physics, 18(12), 8807–8828. https://doi.org/10.5194/acp-18-8807-2018

Luke, E. P., Kollias, P., & Shupe, M. D. (2010). Detection of supercooled liquid in mixed-phase clouds using radar Doppler spectra. Journal of Geophysical Research Atmospheres, 115(19), 19201. https://doi.org/10.1029/2009JD012884

Luke, E. P., Yang, F., Kollias, P., Vogelmann, A. M., & Maahn, M. (2021). New insights into ice multiplication using remote-sensing observations of slightly supercooled mixed-phase clouds in the Arctic. Proceedings of the National Academy of Sciences of the United States of America, 118(13), e2021387118. https://doi.org/10.1073/PNAS.2021387118;WEBSITE:WEBSITE:PNAS-SITE;WGROUP:STRING:PUBLICATION

Morrison, H., De Boer, G., Feingold, G., Harrington, J., Shupe, M. D., & Sulia, K. (2011). Resilience of persistent Arctic mixed-phase clouds Local process interactions in Arctic mixed-phase clouds Modelling and theoretical studies have attempted to explain the counterintuitive persistence of Arctic mixed-phase clouds despite microphysical ins…. NATURE GEOSCIENCE |, 5(1), 11–17. https://doi.org/10.1038/NGEO1332

MOSAiC: International Arctic Drift Expedition 2019-2020 | IARC. (n.d.). Retrieved February 12, 2026, from https://uaf-iarc.org/mosaic-blog/

Moser, M., Voigt, C., Jurkat-Witschas, T., Hahn, V., Mioche, G., Jourdan, O., Dupuy, R., Gourbeyre, C., Schwarzenboeck, A., Lucke, J., Boose, Y., Mech, M., Borrmann, S., Ehrlich, A., Herber, A., Lüpkes, C., & Wendisch, M. (2023). Microphysical and thermodynamic phase analyses of Arctic low-level clouds measured above the sea ice and the open ocean in spring and summer. Atmospheric Chemistry and Physics, 23(13), 7257–7280. https://doi.org/10.5194/acp-23-7257-2023

Murray, F. W. (1967). On the Computation of Saturation Vapor Pressure. Journal of Applied Meteorology, 6(1), 203–204. https://doi.org/10.1175/1520-0450(1967)006<0203:OTCOSV>2.0.CO;2

Nguyen, Q. T., Skov, H., Sørensen, L. L., Jensen, B. J., Grube, A. G., Massling, A., Glasius, M., & Nøjgaard, J. K. (2013). Source apportionment of particles at Station Nord, North East Greenland during 2008-2010 using COPREM and PMF analysis. Atmospheric Chemistry and Physics, 13(1), 35–49. https://doi.org/10.5194/ACP-13-35-2013

Oue, M., Kollias, P., Ryzhkov, A., & Luke, E. P. (2018). Toward Exploring the Synergy Between Cloud Radar Polarimetry and Doppler Spectral Analysis in Deep Cold Precipitating Systems in the Arctic. Journal of Geophysical Research: Atmospheres, 123(5), 2797–2815. https://doi.org/10.1002/2017JD027717

Pasquier, J. T., David, R. O., Freitas, G., Gierens, R., Gramlich, Y., Haslett, S., Li, G., Schäfer, B., Siegel, K., Wieder, J., Adachi, K., Belosi, F., Carlsen, T., Decesari, S., Ebell, K., Gilardoni, S., Gysel-Beer, M., Henneberger, J., Inoue, J., … Zieger, P. (2022). The Ny-Ålesund Aerosol Cloud Experiment (NASCENT): Overview and First Results. Bulletin of the American Meteorological Society, 103(11), E2533–E2558. https://doi.org/10.1175/BAMS-D-21-0034.1

https://doi.org/10.5194/essd-2026-549
Preprint. Discussion started: 10 September 2026

Project Record: Arctic Cloud Summer Expedition (ACSE). (n.d.). Retrieved February 12, 2026, from https://catalogue.ceda.ac.uk/uuid/f4d0cf8f90d240c8bc9556ca4ee075d2/

Radenz, M., Bühl, J., Seifert, P., Griesche, H., & Engelmann, R. (2019). PeakTree: A framework for structure-preserving radar Doppler spectra analysis. Atmospheric Measurement Techniques, 12(9), 4813–4828. https://doi.org/10.5194/amt-12-4813-2019

Shupe, M. D., Matrosov, S. Y., Uttal, T., Shupe, M. D., Matrosov, S. Y., & Uttal, T. (2006). Arctic Mixed-Phase Cloud Properties Derived from Surface-Based Sensors at SHEBA. Journal of the Atmospheric Sciences, 63(2), 697–711. https://doi.org/10.1175/JAS3659.1

Tan, I., Sotiropoulou, G., Taylor, P. C., Zamora, L., & Wendisch, M. (2023). A Review of the Factors Influencing Arctic Mixed-Phase Clouds: Progress and Outlook. 103–132. https://doi.org/10.1002/9781119700357.ch5

Tan, I., & Storelvmo, T. (2019). Evidence of Strong Contributions From Mixed-Phase Clouds to Arctic Climate Change. Geophysical Research Letters, 46(5), 2894–2902. https://doi.org/10.1029/2018GL081871

Tukiainen, S., O'Connor, E., & Korpinen, A. (2020). CloudnetPy: A Python package for processing cloud remote sensing data. Journal of Open-Source Software, 5(53), 2123. https://doi.org/10.21105/joss.02123

Verlinde, J., Rambukkange, M. P., Clothiaux, E. E., McFarquhar, G. M., & Eloranta, E. W. (2013). Arctic multilayered, mixed-phase cloud processes revealed in millimeter-wave cloud radar Doppler spectra. Journal of Geophysical Research Atmospheres, 118(23), 13,199-13,213. https://doi.org/10.1002/2013JD020183

Vogl, T., Radenz, M., Ramelli, F., Gierens, R., & Kalesse-Los, H. (2024). PEAKO and peakTree: tools for detecting and interpreting peaks in cloud radar Doppler spectra - capabilities and limitations. Atmospheric Measurement Techniques, 17(22), 6547–6568. https://doi.org/10.5194/AMT-17-6547-2024

Vüllers, J., Achtert, P., Brooks, I. M., Tjernström, M., Prytherch, J., Burzik, A., & Neely, R. (2021). Meteorological and cloud conditions during the Arctic Ocean 2018 expedition. Atmospheric Chemistry and Physics, 21(1), 289–314. https://doi.org/10.5194/acp-21-289-2021

Wallentin, G., Oertel, A., Ickes, L., Achtert, P., Tesche, M., & Hoose, C. (2025). Sensitivities of simulated mixed-phase Arctic multilayer clouds to primary and secondary ice processes. Atmospheric Chemistry and Physics, 25(13), 6607–6631. https://doi.org/10.5194/acp-25-6607-2025